



Original Full Length Article

Mineralization defects in cementum and craniofacial bone from loss of bone sialoprotein



B.L. Foster^{a,*}, M. Ao^a, C. Willoughby^a, Y. Soenjoya^b, E. Holm^c, L. Lukashova^d, A.B. Tran^a, H.F. Wimer^e, P.M. Zerfas^f, F.H. Nociti Jr.^{a,g}, K.R. Kantovitz^{a,h}, B.D. Quanⁱ, E.D. Sone^{ij,k}, H.A. Goldberg^{b,c,l}, M.J. Somerman^a

^a National Institute of Arthritis and Musculoskeletal and Skin Diseases (NIAMS), National Institutes of Health (NIH), 9000 Rockville Pike, 4120 Building 50, Bethesda, MD 20892, USA

^b Biomedical Engineering Program, Schulich School of Medicine & Dentistry, University of Western Ontario, London, ON N6A 5C1, Canada

^c Department of Biochemistry, Schulich School of Medicine & Dentistry, University of Western Ontario, London, ON N6A 5C1, Canada

^d Hospital for Special Surgery, 535 East 70th Street, New York, NY 10021, USA

^e Department of Vertebrate Zoology, National Museum of Natural History, Smithsonian Institution, Washington, DC, USA

^f Office of Research Services, Division of Veterinary Resources, National Institutes of Health (NIH), 9000 Rockville Pike, 112 Building 28A, MSC 5230, Bethesda, MD 20892, USA

^g Department of Prosthodontics and Periodontics, Division of Periodontics, School of Dentistry, Campinas State University, Piracicaba, SP 13414-903, Brazil

^h Department of Pediatric Dentistry, School of Dentistry, Campinas State University, Piracicaba, SP 13414-903, Brazil

ⁱ Institute of Biomaterials and Biomedical Engineering, University of Toronto, 320A Mining Building, Toronto, ON M5S 3G9, Canada

^j Department of Materials Science and Engineering, University of Toronto, Toronto, ON, Canada

^k Faculty of Dentistry, University of Toronto, Toronto, ON, Canada

^l School of Dentistry, Schulich School of Medicine & Dentistry, University of Western Ontario, London, ON N6A 5C1, Canada

ARTICLE INFO

Article history:

Received 11 February 2015

Revised 21 April 2015

Accepted 2 May 2015

Available online 9 May 2015

Edited by: J. Aubin

Keywords:

Extracellular matrix

Mineralization

Bone

Cementum

Dentin

Cartilage

ABSTRACT

Bone sialoprotein (BSP) is a multifunctional extracellular matrix protein found in mineralized tissues, including bone, cartilage, tooth root cementum (both acellular and cellular types), and dentin. In order to define the role BSP plays in the process of biomineralization of these tissues, we analyzed cementogenesis, dentinogenesis, and osteogenesis (intramembranous and endochondral) in craniofacial bone in *Bsp* null mice and wild-type (WT) controls over a developmental period (1–60 days post natal; dpn) by histology, immunohistochemistry, undecalcified histochemistry, microcomputed tomography (microCT), scanning electron microscopy (SEM), transmission electron microscopy (TEM), and quantitative PCR (qPCR). Regions of intramembranous ossification in the alveolus, mandible, and calvaria presented delayed mineralization and osteoid accumulation, assessed by von Kossa and Goldner's trichrome stains at 1 and 14 dpn. Moreover, *Bsp*^{−/−} mice featured increased cranial suture size at the early time point, 1 dpn. Immunostaining and PCR demonstrated that osteoblast markers, osterix, alkaline phosphatase, and osteopontin were unchanged in *Bsp* null mandibles compared to WT. *Bsp*^{−/−} mouse molars featured a lack of functional acellular cementum formation by histology, SEM, and TEM, and subsequent loss of Sharpey's collagen fiber insertion into the tooth root structure. *Bsp*^{−/−} mouse alveolar and mandibular bone featured equivalent or fewer osteoclasts at early ages (1 and 14 dpn), however, increased RANKL immunostaining and mRNA, and significantly increased number of osteoclast-like cells (2–5 fold) were found at later ages (26 and 60 dpn), corresponding to periodontal breakdown and severe alveolar bone resorption observed following molar teeth entering occlusion. Dentin formation was unperturbed in *Bsp*^{−/−} mouse molars, with no delay in mineralization, no alteration in dentin dimensions, and no differences in odontoblast markers analyzed. No defects were identified in endochondral ossification in the cranial base, and craniofacial morphology was unaffected in *Bsp*^{−/−} mice. These analyses confirm a critical role for BSP in processes of cementogenesis and intramembranous ossification of craniofacial bone, whereas endochondral ossification in the cranial base was minimally affected and dentinogenesis was normal in *Bsp*^{−/−} molar teeth. Dissimilar effects of loss of BSP on mineralization of dental and craniofacial tissues suggest local differences in the role of BSP and/or yet to be defined interactions with site-specific factors.

Published by Elsevier Inc.

* Corresponding author at: National Institutes of Arthritis and Musculoskeletal and Skin Diseases (NIAMS), National Institutes of Health (NIH), Building 50 / Room 4120, Bethesda, MD 20892, USA.

E-mail addresses: brian.foster@nih.gov (B.L. Foster), fnu.aomin@nih.gov (M. Ao), chelseawilloughby15@gmail.com (C. Willoughby), ysoenjoya@uwo.ca (Y. Soenjoya), eholm@uwo.ca (E. Holm), lukashoval@hss.edu (L. Lukashova), anne.tran2@nih.gov (A.B. Tran), helen.wimer@nih.gov (H.F. Wimer), patricia.zerfas@nih.gov (P.M. Zerfas), nociti@unicamp.br (F.H. Nociti), kamilark@yahoo.com.br (K.R. Kantovitz), bryan.quan@utoronto.ca (B.D. Quan), eli.sone@utoronto.ca (E.D. Sone), hagoldbe@uwo.ca (H.A. Goldberg), Martha.somerman@nih.gov (M.J. Somerman).

Introduction

Bone sialoprotein (BSP) is an anionic extracellular matrix (ECM) protein associated with mineralized tissues of the skeleton and dentition [15]. BSP is a member of the Small Integrin Binding Ligand N-linked Glycoprotein (SIBLING) family of multifunctional proteins, also including osteopontin (OPN), dentin matrix protein 1 (DMP1), dentin sialoprotein (DSP), dentin phosphoprotein (DPP), and matrix extracellular phosphoglycoprotein (MEPE) [21,69,77]. Like other SIBLING proteins, BSP contains several highly conserved functional domains. These include an N-terminal collagen-binding domain, an integrin-binding arginine-glycine-aspartic acid (RGD) motif (involved in cell attachment, migration, and cell signaling), and two polyglutamic acid repeats capable of *in vitro* hydroxyapatite (HA) nucleation in coordination with several phosphorylated serine residues [1,2,33,34,85]. These functional domains have been confirmed using *in vitro* approaches, however, the physiological role(s) of BSP in mineralized tissue formation *in vivo* remain elusive and difficult to define.

The functional importance for BSP in the axial skeleton has been the focus of most published *in vivo* studies to date. Mice null for the *Bsp* gene (*Bsp*^{-/-}) feature delayed long bone growth and mineralization, as well as low bone turnover as a consequence of reduced osteoclast formation and activity [11,58,59]. In a femur cortical bone defect model, *Bsp*^{-/-} mice displayed delayed bone repair [60,63], and in a femur bone marrow ablation model, absence of BSP caused both reduced medullary trabecular bone formation and delayed osteoclastic resorption [83]. Investigations focusing on early stages of long bone development identified alterations in the growth plate, delayed initiation of mineralization, and a reduction in expression of some osteogenic markers in *Bsp*^{-/-} vs. WT mice [12,40].

BSP has been identified in the ECM of tooth cementum and dentin as well as in cartilage and bone [15,16,19,26,28,43,57,74]. Previously we identified a developmental defect in cementum in teeth of *Bsp*^{-/-} mice, resulting in the progressive loss of periodontal attachment, disorganization of the periodontal ligament (PDL), and alveolar bone loss at later ages [26]. However, the potential importance of BSP in dentin mineralization remains unclear. While the functional importance of BSP in endochondral bone formation and repair has been confirmed by analysis of long bones, examination of the craniofacial complex can provide insights into the importance of BSP in bone formed by endochondral ossification (e.g. portions of the neurocranium, including synchondroses of the cranial base that contribute to midfacial shape) versus intramembranous ossification (e.g. viscerocranium, including the mandible, alveolus, and frontal calvarial bone).

Our aim in these experiments was to define the functional importance of BSP in dental and craniofacial development, focusing on intramembranous versus endochondral processes of ossification, periodontal ligament (PDL) attachment to the alveolar bone and cementum, and dentin formation.

Materials and methods

Animals

Animal procedures were performed in accordance with guidelines of the Canadian Council on Animal Care and Animal Care and Veterinary Services, University of Western Ontario (London, ON, Canada) and National Institutes of Health (Bethesda, MD, USA). Preparation and genotyping of *Bsp*^{-/-} and wild-type (WT) mice were described previously [26,58], and mice were maintained on a mixed 129/CD1 background. After weaning at three weeks of age, mice were provided both a standard pelleted mouse diet (2018 Tekland Global 18% protein diet, Harlan Laboratories, USA), as well as a soft gel diet (Diet Gel 31M, Clear H₂O, Portland, ME) to reduce incisor malocclusion in homozygous *Bsp*^{-/-} mice. Homozygous WT and *Bsp*^{-/-} littermates were analyzed,

with three to six mice analyzed per genotype at ages 1, 5, 14, 26–30, and 60 days postnatal (dpm).

Histology

Procedures for histology and immunohistochemistry (IHC) were described previously for Bouin's fixed, decalcified, paraffin-embedded samples [23,24]. For undecalcified histology, tissues were processed and methylmethacrylate-embedded for automated microtome sectioning (6 μm) for Goldner's trichrome and von Kossa staining [46].

IHC employed biotinylated secondary antibodies and peroxidase substrate. Primary antibodies included polyclonal rabbit anti-BSP (1:200; Renny Franceschi, University of Michigan, Ann Arbor) [26], monoclonal rat IgG anti-tissue nonspecific alkaline phosphatase (1:200; R&D Systems, Minneapolis, MN) [88], polyclonal LF-175 rabbit anti-osteopontin (1:200; Larry Fisher, NIDCR) [25], polyclonal rabbit IgG anti-osterix/SP7 (1:100; Abcam, Cambridge, MA), polyclonal rabbit anti-osteocalcin (1:1000; Clontech Laboratories Inc., Mountain View, CA), and polyclonal goat IgG anti-RANKL (1:50; Santa Cruz Biotechnology, Santa Cruz, CA) [26]. Tartrate resistant acid phosphatase (TRAP) staining was performed on decalcified and deparaffinized tissues according to manufacturer's instructions (Wako Chemical, Japan).

Transmission electron microscopy (TEM)

TEM was performed at two different facilities (14 dpm at NIH and 27–30 dpm at University of Toronto). For 14 dpm samples, mandibles were fixed in 2% paraformaldehyde, 0.5% glutaraldehyde in phosphate buffered saline (PBS) for 48 h, and washed in cacodylate buffer. Next, tissues were serially dehydrated in alcohol, embedded in LR white resin (Electron Microscopy Sciences, Hatfield, PA) and UV polymerized for 8 h. Thin sections (80 nm) were obtained from buccal and lingual aspects of the first maxillary and mandibular molars using a Leica Ultracut-UCT ultramicrotome (Leica Microsystems, Deerfield, IL), placed onto 300-mesh copper grids, and stained with saturated uranyl acetate in 50% methanol followed by lead citrate. Samples were viewed with a JEM-1200EXII electron microscope (JEOL, Tokyo, Japan) at 80 kV, and images were captured using a XR611M, mid-mounted, 10.5 megapixel CCD camera (Advanced Microscopy Techniques, Danvers, MA).

For 27–30 dpm samples, freshly dissected mandibles were fixed overnight at 4 °C in 0.8% formaldehyde and 0.2% glutaraldehyde in PBS. For both mineralized and demineralized tissues, sections were obtained from the lingual aspect of the first molar. For examination of natively mineralized tissues, samples from 27 dpm mice were washed with water, dehydrated in an ethanol gradient followed by propylene oxide, and embedded in Embed 812 resin (Electron Microscopy Sciences). Sections (~90 nm thick) were cut using a Leica Ultracut ultramicrotome, transferred to carbon-coated formvar Ni grids and examined unstained. For examination of demineralized tissues, fixed mandibles from 30 dpm mice were demineralized for 7 days in PBS containing 12.5% EDTA (pH 7.4), 0.2% paraformaldehyde, and 0.05% glutaraldehyde at 4 °C with rocking and daily solution change. The mandibles were then infiltrated with several changes of 2.3 M sucrose, frozen, and sectioned on a Leica EM UC6-NT ultracryomicrotome at -90 °C. Sections (~210 nm thick) were transferred to Ni grids supported by carbon-coated formvar and stained with 2% uranyl acetate in water for 5 min, and washed in water. For both mineralized and demineralized sections, grids were imaged on an FEI Technai 20 TEM operating at 200 kV with an AMT 16000-S CCD camera.

Microcomputed tomography (microCT)

For dentoalveolar imaging, dissected and formalin-fixed mandibles were scanned on a Scanco Medical microCT 50 (Scanco Medical AG, Brüttisellen, Switzerland) with parameters of 9 μm voxel size, 55 kVp, 145 mA, with 0.36 degree rotation step (180 degree angular range)

and a 400 ms exposure per view. Exported DICOM files were reoriented using ImageJ software (1.48r), with comparable coronal, sagittal, and transverse planes of section chosen for image comparison.

For craniofacial analysis, formalin-fixed crania ($n = 5$ per genotype per age for 5, 14, and 26 dpn) were scanned in 70% ethanol on a Scanco μ CT 35 (Scanco Medical, Brüttisellen, Switzerland) with parameters: 15 μ m voxel size, 55 kVp, 145 mA, with 0.36 degree rotation step (180 degree angular range), and 400 ms exposure per view. Scanco μ CT software (HP, DECwindows Motif 1.6) was used for 3D reconstruction and image viewing. After 3D reconstruction, volumes of parietal bone were contoured and segmented using a global threshold of 0.25 g HA/cm³. Directly measured tissue volume (TV), and bone volume (BV), as well as bone volume fraction (BV/TV), bone thickness and tissue mineral density (TMD) were calculated.

Craniofacial and suture measurements

Craniofacial linear measurements were made on 3D reconstructed microCT scans of *Bsp*^{-/-} and WT mouse crania at 5, 14, and 26 dpn ($n = 5$ per genotype at all ages). Measurements were made using skeletal landmarks employed previously for craniofacial morphometry [53,71] and standard procedures employed by Jackson Laboratories for documenting craniofacial phenotypes; http://craniofacial.jax.org/new_standard_protocols.html. Measurements included: skull length (nasale to paro), skull width (measured between the right and left intersections between the squamosal body and the zygomatic process of the squamous portion of the temporal bone), skull height (modified due to removal of the mandible), nose length (nasale to bregma), nasal bone length (measured from nasale to nasion), upper jaw length, lengths of frontal and parietal bones, width of the premaxilla, distance between lateral margins of right and left lacrimal bones (lacrimal width), and distance between lateral margins of right and left squamosal bones (squamosal width).

Suture widths were measured on 3D reconstructed microCT scans of *Bsp*^{-/-} and WT mouse crania at 5, 14, and 26 dpn ($n = 5$ per genotype at all ages). Sutures measured included: Sagittal, frontal, lambdoid (right and left sides), and coronal (right and left sides). Additionally, widths of the anterior and posterior fontanelles were measured.

Quantitative polymerase chain reaction (QPCR)

Tissues were isolated from WT or *Bsp*^{-/-} mice in order to isolate total RNA for gene expression analysis. For PDL, first mandibular molars were removed from mandibles at 5, 14, and 26 dpn (with care to exclude gingiva and bone) and RNA was harvested from attached soft tissues using a lysis buffer and purification kit, according to manufacturer's directions (RNeasy, Qiagen, Valencia, CA). For mandibular bone, molar and incisor teeth were removed from jaws, and bone remaining was stored in RNAlater (Thermo Fisher Scientific, Waltham, MA) at -80°C . For calvarial bone at 14 and 26 dpn, portions of the parietal and frontal bones and the intervening sutures were removed and stored in RNAlater at -80°C . Bones were homogenized with a lysing matrix of zirconium spheres and garnet flakes using a high-speed bench top homogenizer (FastPrep-24, MP Biomedicals, Santa Ana, CA), at 3 cycles of 4000 rpm for 30 s, on dry ice. Total RNA was isolated from homogenates with TriPure isolation reagent, following manufacturer's recommendations (Roche Applied Science, Indianapolis, IN). RNA was used for cDNA synthesis, and 1 μ g of cDNA was used as template for quantitative PCR or PCR array on a Lightcycler 2.0 system (Roche Applied Science). PCR primers for mouse transcripts included *Acp5* (NM_001102404.1): Forward—CAGCTCAGTTGGGTAGCA CA and Reverse—CGTCCTCAAAGGTCTCTGG; *Alpl* (NM_007431.3): F—GGGACATGCAGTATGAGTT and R—GGCCTGGTAGTTGTTGTGAG; *Ctsk* (NM_007802.4): F—GCACCCTTAGCTCTCCGCTC and R—ACCCACAT CCTGCTGTTGAG; *Fgfr1* (NM_001079908.2): F—GACTCTGGCCTCTACG CTTG and R—TAGGGAGCTACAGGCCTACG; *Fgfr2* (NM_010207.2):

F—CACGACCAAGAAGCCAGACT and R—CTCGGCCGAAACTGTACCT; *Fgfr3* (NM_001163215.2): F—GCGACAGGTGCTCTGGAAT and R—GCCAGAACAGGACCTTCTCC; *Gli1* (NM_010296.2): F—CCGACGGA GGTCTCTTTGTC and R—AACATGGCGTCTCAGGGAAG; *Msx2* (NM_013601.2): F—GCCTCGGTCAAGTCGGAAAA and R—GGTCATATGCTG GGCGG; *Sp7* (*Osterix*; NM_130458.3): F—TGCTTCCAATCTATTTCG and R—AGCTCAGGGGAATCGAG; *Spp1* (*Opn*; NM_001204201.1): F—TTTACAGCCTGCACCC and R—CTAGCAGTGACGGTCT; proprietary *Tnfrsf11* (*Rankl*; NM_011613.3) primers included in a PCR array (Qiagen); *Tnfrsf11a* (*Rank*; NM_009399.3): F—AGTCTGTGATCAGGC AAGG and R—CCGTATCCTTGTGAGCTGC; and *Twist1* (NM_011658.2): F—GCCGGAGACCTAGATGTCATTG and R—CCACGCCCTGATTCTTGTA.

Results

BSP localization in developing craniofacial bones and teeth

To inform the developmental analysis of loss of BSP in craniofacial tissues, localization of BSP protein was analyzed in craniofacial and dental tissues from ages 1 to 14 days postnatal (dpn). During both crown and root formation, little BSP protein was identified by immunohistochemistry (IHC) in odontoblasts or dentin ECM (Figs. 1A, B, D, E). During root formation, BSP was concentrated in the acellular cementum lining the tooth root surface (Fig. 1E). Bones forming through intramembranous ossification, e.g. alveolus, mandible, and calvaria, were positive for BSP (Figs. 1G–O). Endochondral bone of the sphenoccipital synchondrosis (SOS) of the midline cranial base exhibited BSP staining (Figs. 1P, Q), as did the pre-sphenoidal synchondrosis (PSS; data not shown). Absence of BSP immunostaining was confirmed in *Bsp*^{-/-} mice for all tissues analyzed (Figs. 1C, F, I, L, O, and R).

Defective intramembranous bone mineralization in *Bsp* null mice

We examined mandibular, alveolar, and calvarial bones to determine the effect of loss of BSP on craniofacial bones formed by intramembranous ossification. At 1 dpn, the early mandible appeared similar in dimension and organization in *Bsp*^{-/-} versus WT, as observed by picosirius red staining for collagen, with and without polarized light microscopy (Figs. 2A–D). Histology and von Kossa staining of the alveolus surrounding the molar tooth bud, the basal bone of the mandible, and the coronal suture region between the frontal and parietal bones identified delays in mineralization at all of these sites in *Bsp*^{-/-} mice, compared to controls (Figs. 2E–P). Alveolar and mandibular bone, in particular, featured extensive regions of unmineralized osteoid accumulation, typically more than 200–300 μ m long by more than 100 μ m wide. The delay in mineralization persisted at 14 dpn, where Goldner's trichrome staining identified osteoid on the surfaces of bone of the alveolar crest and molar root furcation region, often 20–30 μ m in thickness (Figs. 2Q–T). Osteoid was recognizable on alveolar bone surfaces at ages of 26 and 60 dpn by histology (data not shown).

Parietal bones of the cranium were analyzed further by microCT to determine whether loss of BSP affected mineralization of these bones. No significant differences were found in *Bsp*^{-/-} versus WT mice for bone thickness, BV/TV, or TMD at 5 dpn (Supplementary Table 1), suggesting no major mineralization deficiency in the parietal bone proper at this early age. By 14 dpn, *Bsp*^{-/-} parietal bone was significantly thicker (10%; $p < 0.05$), and BV/TV trended towards increase, while TMD trended towards decrease in *Bsp*^{-/-} mice compared to controls. At 26 dpn, parietal bone thickness, BV/TV, and TMD were all significantly increased in *Bsp*^{-/-} mice (by 27%, 8%, and 7%, respectively). The observations of increased thickness, BV/TV, and TMD in *Bsp*^{-/-} mice parietal bones versus controls at 14 and 26 dpn indicate no lasting mineralization delay or defect, and are consistent with effects from reduced osteoclast activity documented in vivo and in vitro [58,83].

Because delayed mineralization was identified by histology at the coronal suture at 1 dpn, we measured cranial suture widths at 5, 14,

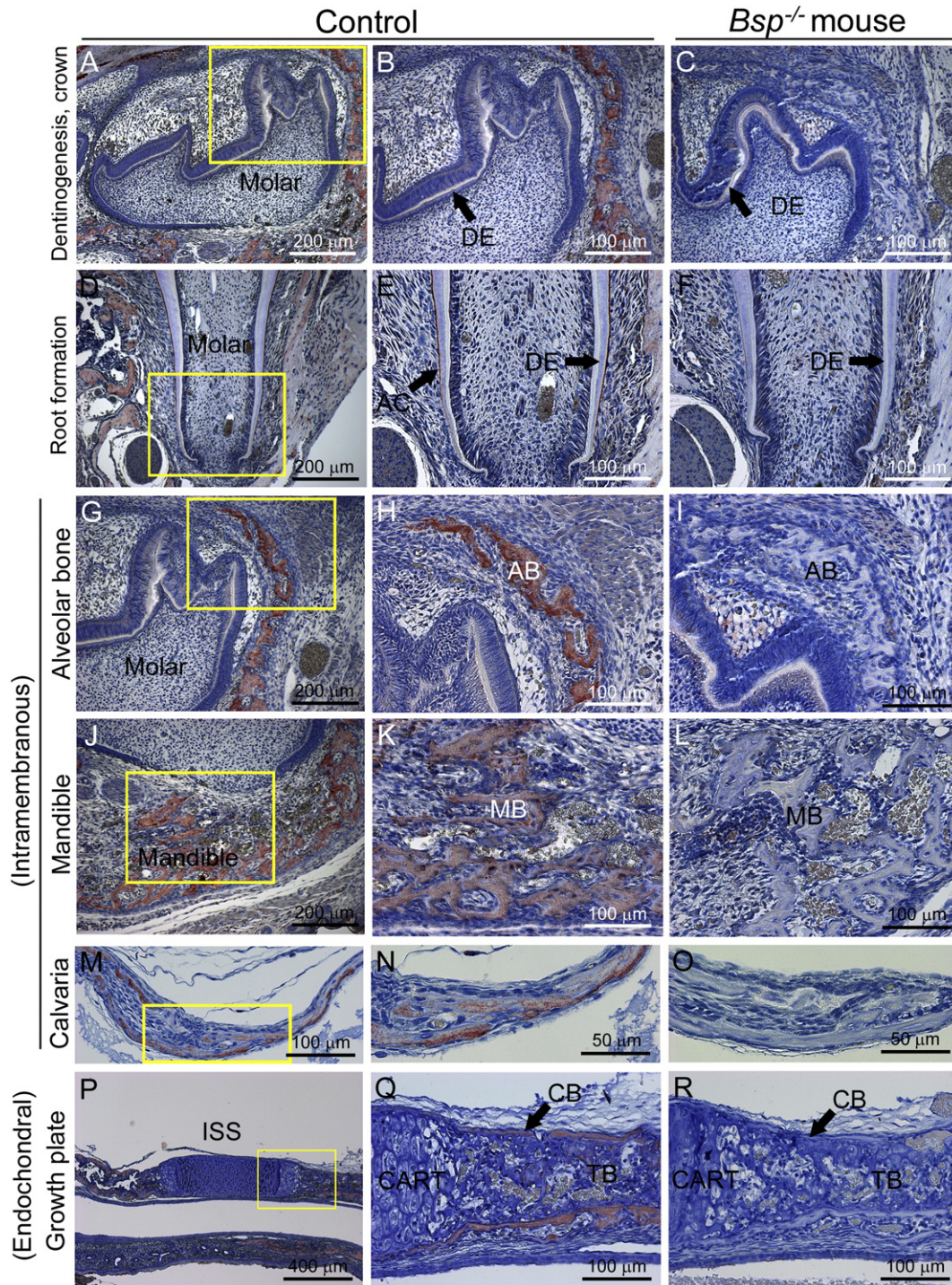


Fig. 1. BSP localization in dentinogenesis and craniofacial osteogenesis. While BSP is localized in negligible concentrations by IHC in dentin (DE) during molar tooth crown (A, B) and root (D, E) formation, the protein is concentrated in the acellular cementum (AC). BSP is also detected during craniofacial intramembranous ossification of the (G, H) alveolar bone (AB), (J, K) mandibular bone (MB), and (M, N) calvarial bone, as well as (P, Q) both cortical and trabecular bones (CB and TB, respectively) arising from cartilage (CART) via endochondral ossification, as in the intersphenoid synchondrosis (ISS) of the cranial base. There is a lack of BSP immunostaining in all of these tissues in comparable sections from *Bsp*^{-/-} mice, demonstrated in panels C, F, I, L, O, and R. Panels A–C and G–R are from 1 dpn mice, and panels D–F are from 14 dpn mice. Yellow boxes in first column panel indicate areas shown under higher magnification in panels in the second column.

and 26 dpn. At 5 dpn, the coronal suture was significantly larger by 65% ($p < 0.01$) and the lambdoidal suture was significantly increased by 20% ($p < 0.05$) in *Bsp*^{-/-} mouse crania compared to WT (Table 1; Figs. 2U–V). Sagittal and frontal sutures trended towards increased mean widths in *Bsp*^{-/-} versus WT mice as well. Additionally, the anterior fontanelle width was significantly increased by 40% in *Bsp*^{-/-} versus WT mice, while the posterior fontanelle trended towards increased

width in *Bsp*^{-/-} mice. By 14 dpn, differences in sutures and fontanelles in *Bsp*^{-/-} versus WT mice were no longer observed. Surprisingly, by 26 dpn, *Bsp*^{-/-} mouse crania featured significantly reduced sagittal, coronal, and lambdoidal sutures, while anterior and posterior fontanelle widths trended towards reduction as well. This pattern suggests that early mineralization deficiencies reflected in suture widths normalized and then reversed at later ages.

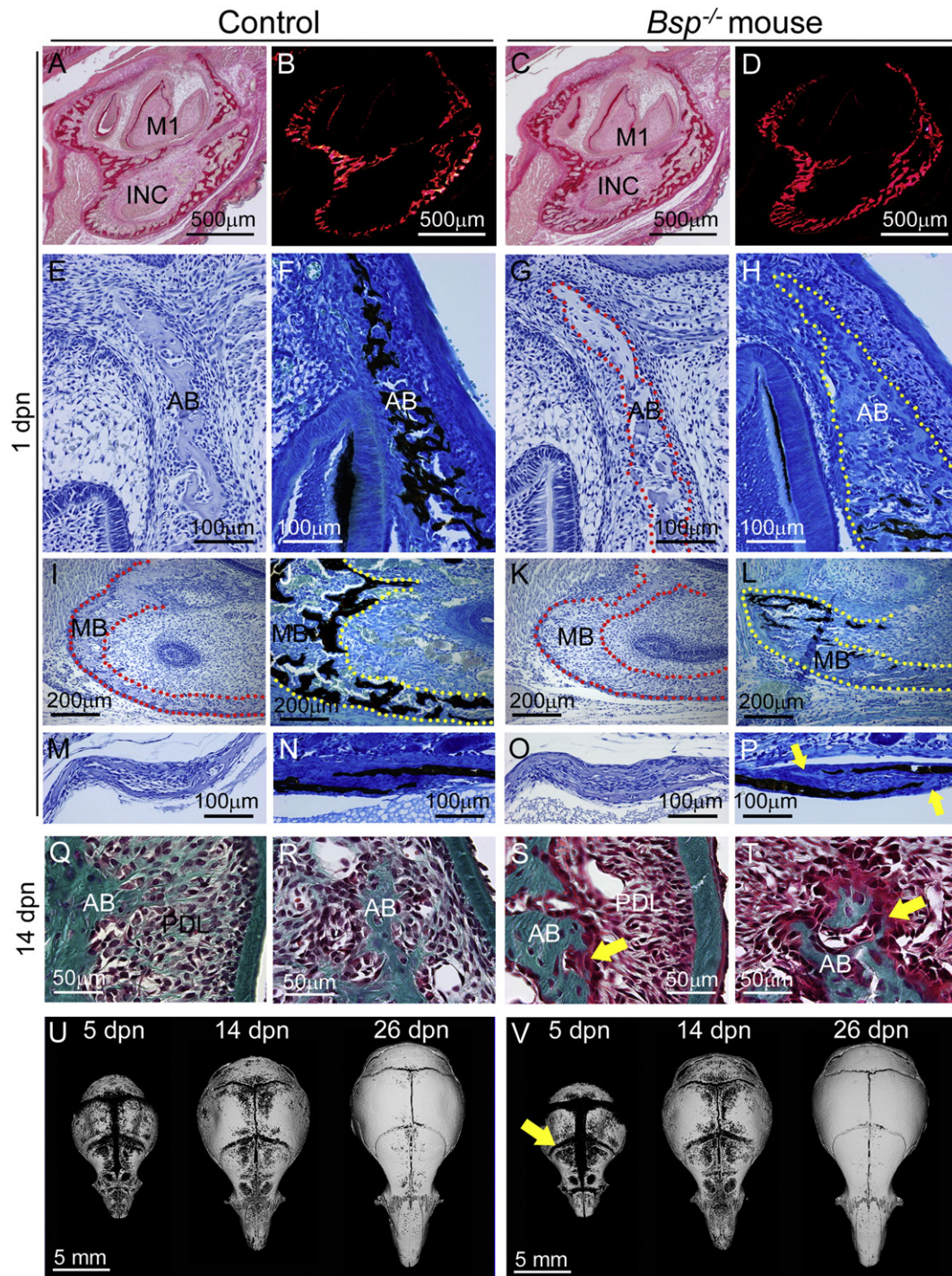


Fig. 2. Defective intramembranous ossification with loss of BSP. Compared to (A, B) 1 dpn WT mandibles stained by picosirius red and observed under polarized light, (C, D) *Bsp*^{-/-} mandibles are similar in size and collagen deposition and organization. Compared to 1 dpn WT, regions of unmineralized osteoid are observed during formation of (E–H) alveolar bone (AB), (I–L) mandibular bone (MB), and (M–P) calvarial bone (at the coronal suture). H&E images are paired with similar von Kossa stained sections, and yellow and red stippled lines are used to define bone borders. Lack of mineralization in *Bsp*^{-/-} versus control mice is shown by lack of silver (black) staining, with yellow arrows indicating areas of osteoid in calvaria (P). At 14 dpn, compared to (Q, R) WT, alveolar bone in the (S, T) *Bsp*^{-/-} mandible features presence of extensive osteoid (yellow arrows). (U, V) MicroCT isosurface images of the cranial vault show that compared to WT, *Bsp*^{-/-} mice feature wider sutures and fontanelles at 5 dpn (for example, the yellow arrow indicating wider coronal suture), no apparent differences at 14 dpn, and more closed sutures by 26 dpn. Table 1 summarizes suture and fontanelle measurements.

While fusion of the sutures was not observed in *Bsp*^{-/-} mice by 26 dpn, we nonetheless analyzed several genes associated with craniosynostosis to determine if these were dysregulated in cranial bones at 14 and 26 dpn. These included *Fgfr1*, *Fgfr2*, *Fgfr3*, *Gli1*, *Msx2*, and *Twist1* [36,70,87]. While we found trends towards mild reduction in most of these genes in *Bsp*^{-/-} vs. WT mouse calvaria, no significant

differences were identified (Supplementary Fig. 1A). Osteoblast markers *Alpl*/TNAP and *Spp1*/OPN were significantly decreased in *Bsp*^{-/-} versus WT samples at 14 dpn (with similar trends at 26 dpn) (Supplementary Fig. 1B), likely reflecting reduced expression of osteoblast markers reported previously in long bones [40,58]. Because *Bsp*^{-/-} mice feature reduced long bone remodeling due to loss of osteoclast activation

Table 1

Cranial suture measurements of *Bsp*^{-/-} versus WT mice. Measurements of cranial sutures were made on 3D microCT reconstructions of WT and *Bsp*^{-/-} mice at 5, 14, and 26 dpn (n = 4–5 for each genotype and age). Values are reported as mean ± SD.

	5 dpn		14 dpn		26 dpn	
	WT	<i>Bsp</i> ^{-/-}	WT	<i>Bsp</i> ^{-/-}	WT	<i>Bsp</i> ^{-/-}
Sagittal suture width (mm)	0.49 ± 0.12	0.61 ± 0.20	0.18 ± 0.04	0.15 ± 0.03	0.11 ± 0.02	0.03 ± 0.05*
Frontal suture width (mm)	0.49 ± 0.06	0.67 ± 0.19	0.33 ± 0.08	0.29 ± 0.05	0.14 ± 0.03	0.32 ± 0.39
Lambdoidal suture width (mm)	0.42 ± 0.07	0.51 ± 0.04*	0.20 ± 0.06	0.20 ± 0.03	0.19 ± 0.09	0.01 ± 0.03*
Coronal suture width (mm)	0.32 ± 0.05	0.53 ± 0.12**	0.41 ± 0.05	0.44 ± 0.06	0.19 ± 0.03	0.02 ± 0.05**
Anterior fontanelle width (mm)	0.38 ± 0.05	0.54 ± 0.09**	0.33 ± 0.06	0.31 ± 0.07	0.12 ± 0.14	0.00 ± 0.00
Posterior fontanelle width (mm)	0.71 ± 0.15	0.95 ± 0.21	0.30 ± 0.04	0.31 ± 0.03	0.25 ± 0.04	0.13 ± 0.09

* p < 0.05 by independent samples *t*-test.

** p < 0.01 by independent samples *t*-test.

[11,58], we also assayed osteoclast markers in calvarial bones, including *Acp5* (gene for tartrate resistant acid phosphatase; TRAP), *Ctsk* (gene for cathepsin K), and *Tnfrsf11a* (gene for receptor activator of NF- κ B, RANK). Expression of *Acp5* and *Tnfrsf11a* were significantly reduced in *Bsp*^{-/-} vs. WT mouse calvaria at 14 dpn, with a similar trend at 26 dpn, and the same non-significant trend in *Ctsk* mRNA (Supplementary Fig. 1C). Overall, involvement of craniosynostosis genes in the suture alterations in *Bsp*^{-/-} mice could not be ruled in or out, however reductions in osteoclast markers suggests reduced osteoclast activity may contribute to decreased suture widths [3,51].

Because alveolar and mandibular bone presented severe mineralization defects in the absence of BSP, these bones were selected for additional analysis. Alterations in osteoblast markers have been reported in long bones of *Bsp*^{-/-} mice [12,40]. Osteoblast markers including OSX, TNAP, and OPN were assayed in alveolar and mandibular bone by IHC at 1 dpn. Expression of OSX, a transcription factor directing the osteoblast differentiation program, was not affected by loss of BSP (Figs. 3A–D and I–L). TNAP appeared to be increased around alveolar and mandibular bone (Figs. 3E, G, M, and O), consistent with increased circulating serum ALP activity reported in 3–8 week-old *Bsp*^{-/-} mice [26]. OPN was localized to bone matrix and cells in a similar manner in *Bsp*^{-/-} and WT mice (Figs. 3F, H, N, and P). Quantitative PCR did not detect differences in transcripts for *Sp7* (OSX), *Alpl* (TNAP), or *Spp1* (OPN) in *Bsp*^{-/-} versus WT alveolar/mandibular bone samples harvested at 5 dpn (Figs. 3Q–S), during the time period when these tissues were severely hypomineralized.

Periodontal defects in *Bsp* null mice

Alveolar bone is part of the periodontal attachment complex, functioning as a unit with the root cementum and PDL, to anchor the tooth. Embedding of Sharpey's fibers of the PDL into both alveolar bone and cementum is critical for periodontal function, and we reported previously that reduced acellular cementum in *Bsp*^{-/-} mice caused loss of PDL attachment [26]. To characterize this deficiency in more detail, scanning electron microscopy (SEM) and transmission electron microscopy (TEM) were employed. The acellular cementum defect is observed by SEM as the absence of a mineralized cementum layer surrounding root dentin in *Bsp*^{-/-} mouse molars at 30 dpn (Figs. 4A–B), with resorption pits noted on the root surface (asterisk in Fig. 4B).

Using TEM, we examined tooth root surfaces at two stages of root formation including 14 dpn (early root formation) and 27–30 dpn (later root formation). At 14 dpn, the mineralized collagen fringe fibers that serve as the dental cementum matrix were apparent in molar root sections as a 0.5–1 μ m thick layer at the interface of the PDL and root dentin, continuous with collagen fibrils extending into the PDL space (Fig. 4C). In unstained WT sections at 27 dpn, acellular cementum was observed as an approximately 2 μ m layer adjacent to the mantle dentin layer (Fig. 4D). In *Bsp*^{-/-} molars at both ages, dental cementum ultrastructure was absent, resulting in an abrupt transition from dentin to PDL (Figs. 4E–F). PDL detachment from the root was prevalent in

Bsp^{-/-} molars at both ages examined, however, in regions where the ligament remained attached, the PDL appeared relatively normal despite the aberrant root surface topology (Supplementary Fig. 2).

In contrast to the defects observed on the tooth root, insertion of Sharpey's fibers into *Bsp*^{-/-} mouse alveolar bone was evident by TEM and did not appear different from WT (Figs. 4G–H). Notably, tearing at the bone–PDL interface was generally not observed in *Bsp*^{-/-} mice, while prevalent cementum–PDL interfacial tearing indicated a structural defect at the tooth root surface. Picrosirius red staining confirmed that the integrity of the collagen fibers entering the alveolar bone were similar in WT and *Bsp*^{-/-} tissues at 14 dpn, though the PDL of the *Bsp*^{-/-} tooth already was disrupted from lack of cementum formation and subsequent attachment (Fig. 4I vs. K). By 26 dpn, though the collagen fibers traveling through the alveolar bone were still apparent in *Bsp*^{-/-} mouse, bone resorption had degraded the structure of the PDL–bone interface, and little collagen organization was apparent in the PDL space (Figs. 4J and L).

Increased bone resorption in *Bsp* null alveolar and mandibular bone

Bone turnover in *Bsp*^{-/-} mouse long bones was reported to be low due to reduced osteoclast differentiation [11,58,83]. At advanced ages, *Bsp*^{-/-} mice feature severe alveolar and mandibular bone loss (Supplementary Fig. 3 and [26]). To further define the mechanism of this underlying discrepancy and to understand how it corresponds to the observed mineralization defects in the *Bsp*^{-/-} mouse craniofacial bone, we examined receptor activator of NF- κ B ligand (RANKL) by immunostaining and QPCR, and tartrate resistant acid phosphatase (TRAP) staining in mandibles from 1 to 60 dpn. IHC revealed no obvious differences in RANKL at early ages (1 and 14 dpn), with increased RANKL staining in the periodontal region of *Bsp*^{-/-} mice at 26 and 60 dpn (Figs. 5A–H), after the molar was erupted and in occlusion, and coincident with observations of PDL detachment from the root surface. QPCR data from PDL tissues showed that *Bsp*^{-/-} mice featured significantly reduced *Tnfrsf11* (RANKL) at 5 dpn, equivalent expression to WT at 14 dpn, and more than 4-fold significantly increased *Tnfrsf11* at 26 dpn (Fig. 5M), matching the pattern of RANKL IHC.

TRAP staining was used to enumerate osteoclast-like cells in alveolar and mandibular bone (Figs. 5I–L). At 1 and 14 dpn, *Bsp*^{-/-} mandibles in general, and alveolar bone in particular, featured similar or reduced numbers of osteoclasts compared to WT (Figs. 5N–O). However, by 26 dpn, *Bsp*^{-/-} alveolar bone featured 2-fold significantly increased number of osteoclasts compared to WT tissues (p < 0.05). By 60 dpn, the number of osteoclasts in *Bsp*^{-/-} mouse alveolar and alveolar/mandibular bone was significantly increased over WT, by 8-fold and 3-fold, respectively (p < 0.05 and p < 0.01, respectively).

Dentinogenesis is unaffected in *Bsp* null mouse molars

Odontoblasts that produce tooth dentin arise from cranial neural crest ectomesenchyme, and therefore have a common origin with

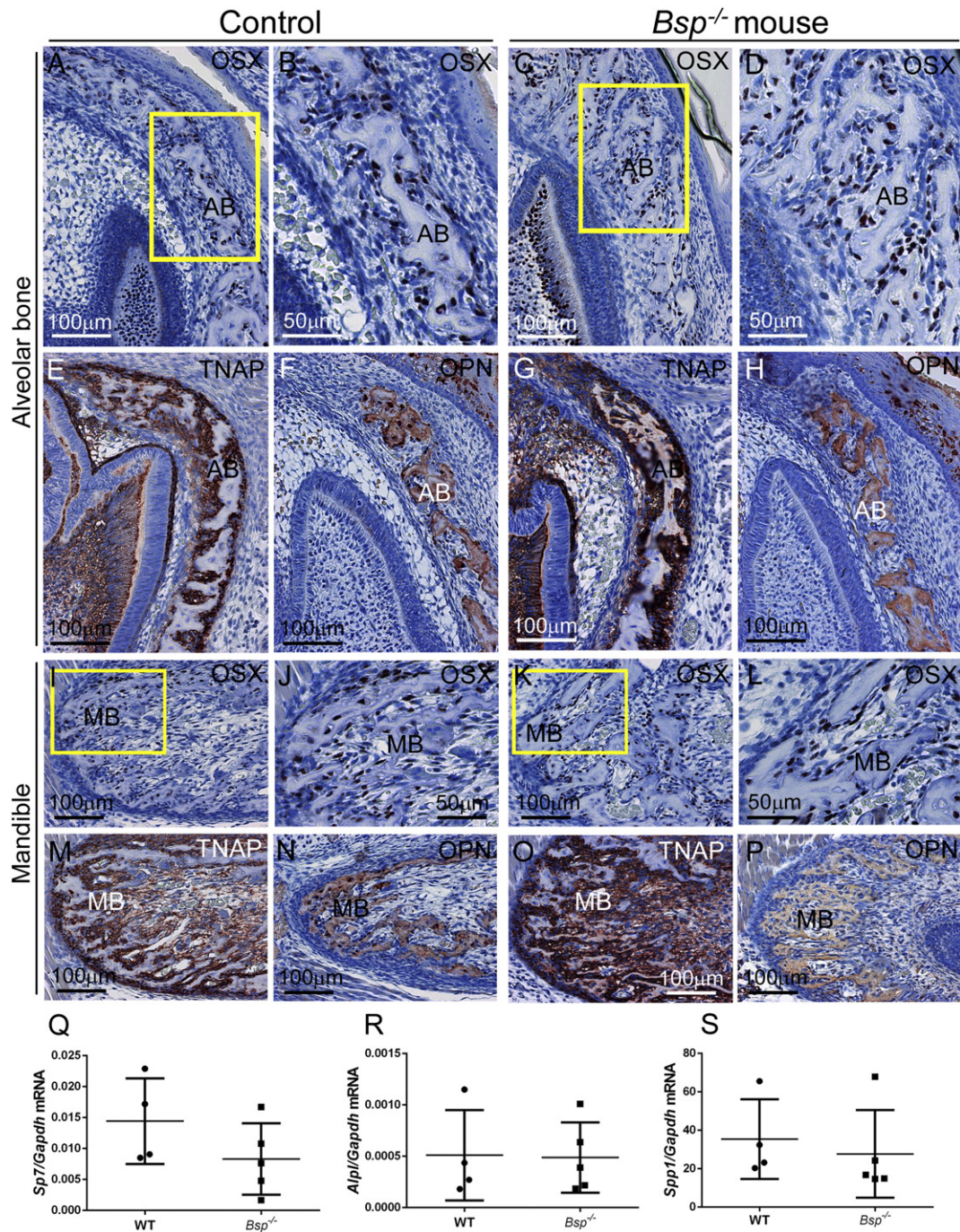


Fig. 3. Comparison of osteoblast markers in intramembranous ossification in *Bsp* null versus controls. Osteoblast markers were assayed in regions of (A–H) alveolar and (I–P) mandibular bone formation in WT and *Bsp*^{-/-} mice at 1 dpn. (A–D, I–L) No differences in early osteoblast marker osterix (OSX) are observed in *Bsp* null compared WT, with OSX-positive cells covering bone surfaces. Yellow boxes in A and C indicate areas shown under higher magnification in B and D, respectively. Yellow boxes in I and K indicate areas shown under higher magnification in J and L, respectively. (E, G and M, O) Tissue nonspecific alkaline phosphatase (TNAP) is present at bone surfaces in WT and *Bsp* null bones compared to WT, with some suggestion of increased TNAP at certain locations in *Bsp*^{-/-} mice versus WT. (F, H and N, P) Osteopontin (OPN) is similarly distributed in bone matrix of alveolar and mandibular bone in WT and *Bsp*^{-/-} mice. (Q–S) Quantitative PCR on mRNA from 5 dpn WT and *Bsp*^{-/-} mandibles indicated no significant differences ($p > 0.05$ for $n = 4$ –5 samples) in expression of *Sp7* (Osterix), *Alpl* (TNAP), or *Spp1* (OPN).

osteoblasts and cementoblasts of the periodontia. To determine effects of loss of BSP on dentin, dentinogenesis in tooth crown and root of *Bsp*^{-/-} mice was examined. At 1 dpn, initiation of mineralization of the crown dentin matrix of the first mandibular molar was noted, indicated by differential von Kossa and Goldner's trichrome stains (Figs. 6A–H). Initiation of crown dentin mineralization was comparable in *Bsp*^{-/-} and WT mouse molars. Ongoing dentinogenesis was analyzed in molar roots. Parameters measured included the width of predentin and dentin

layers (in 14 and 26 dpn molars) and the lag in mineralization between predentin matrix secretion and its mineralization to dentin (at 14 dpn). No observational or statistical differences in dentinogenesis were observed between *Bsp*^{-/-} mice and WT controls in any histomorphometric parameters measured, suggesting no defects in processes of dentin secretion or mineralization (Figs. 6I–L, M, O, and R).

Molars were analyzed by TEM at 27 dpn to further explore the collagen-mineral ultrastructure of dentin. Imaging and diffraction of

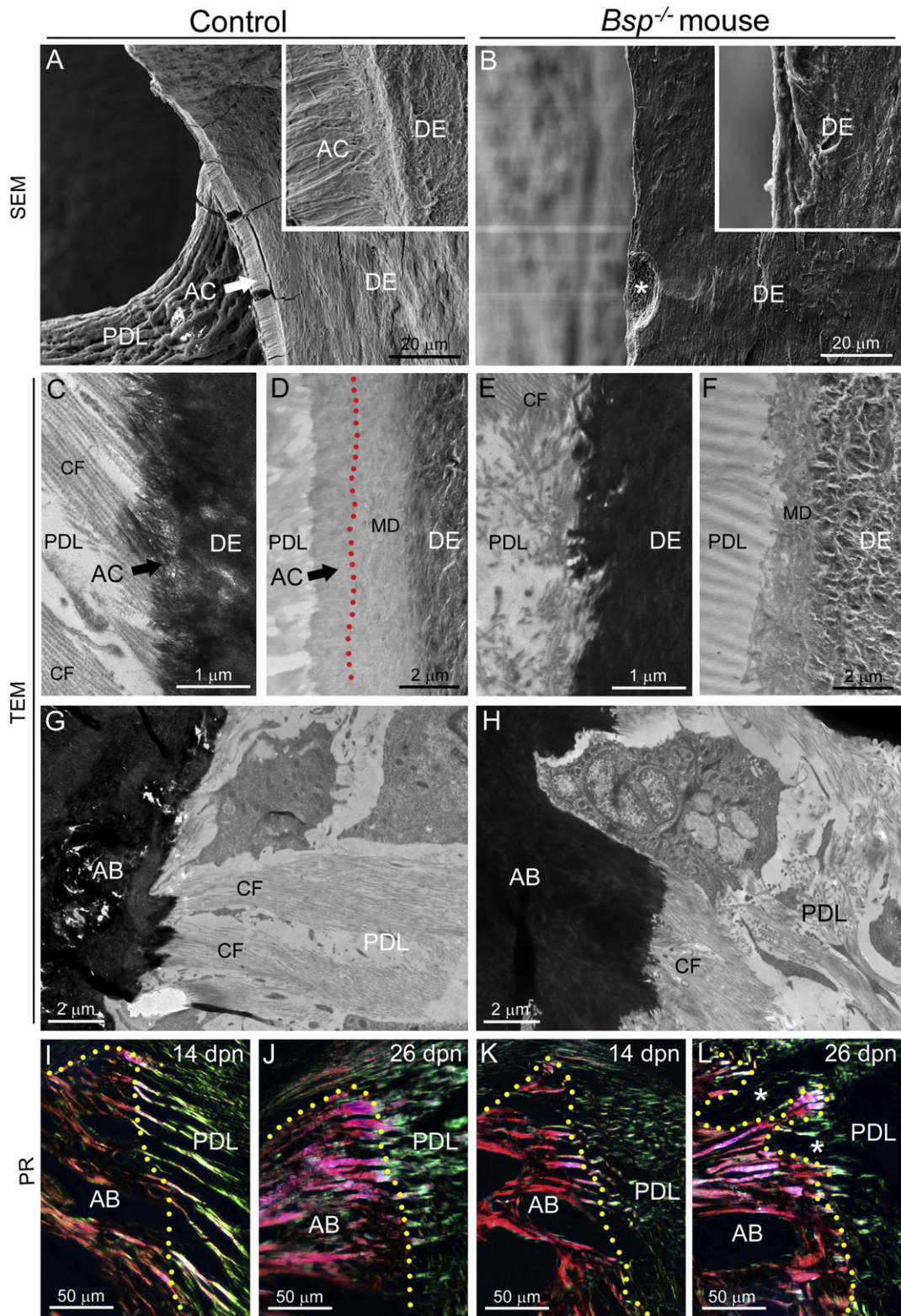


Fig. 4. Defective cementum and periodontal ligament attachment in *Bsp* null mouse molars. Compared to the well-developed acellular cementum (AC) in the (A) WT mouse molar at 30 dpn, SEM in back-scattered mode reveals that (B) *Bsp*^{-/-} mouse molars do not feature a recognizable cementum layer on the dentin (DE) root surface, and no attached periodontal ligament (PDL) is observed on these molars. Insets show high magnification images of WT and *Bsp*^{-/-} molar root surfaces at equivalent magnification. Note a feature (*) consistent with a resorption pit on the *Bsp*^{-/-} mouse root surface. TEM was applied to (C, E) 14 dpn and (D, F) 27 dpn natively mineralized sections of molar teeth. TEM of uranyl acetate stained sections at 14 dpn reveals the (C) progressive mineralization of Sharpey's fibers marking cementogenesis on the WT molar surface, and a well-aligned collagen fibers (CF) of the periodontal ligament (PDL), while (E) the *Bsp*^{-/-} mouse displays a severely disrupted root surface topography, absence of Sharpey's fiber development, and disarray in the adjacent PDL collagen fibers. At 28 dpn, (D) unstained root surfaces in WT mice feature layers of dentin, outermost mantle dentin (MD), and acellular cementum (mantle dentin–cementum interface is indicated by red stippled line), whereas (F) *Bsp*^{-/-} mouse molars feature no layer of acellular cementum adjacent to mantle dentin, resulting in a disrupted dentin–PDL interface. The normal insertion of Sharpey's fibers into the alveolar bone surface in (G) WT control mice is not perturbed in (H) *Bsp*^{-/-} mice. Picrosirius red (PR) staining under polarized light confirms dense insertion of large-sized collagen fibers from the PDL into the alveolar bone of (I, J) WT and (K, L) *Bsp*^{-/-} mouse. Areas of bone loss (white stars in L) are apparent in *Bsp*^{-/-} mouse alveolar bone by 26 dpn. The margin of the alveolar bone in I–L is indicated by a yellow stippled line.

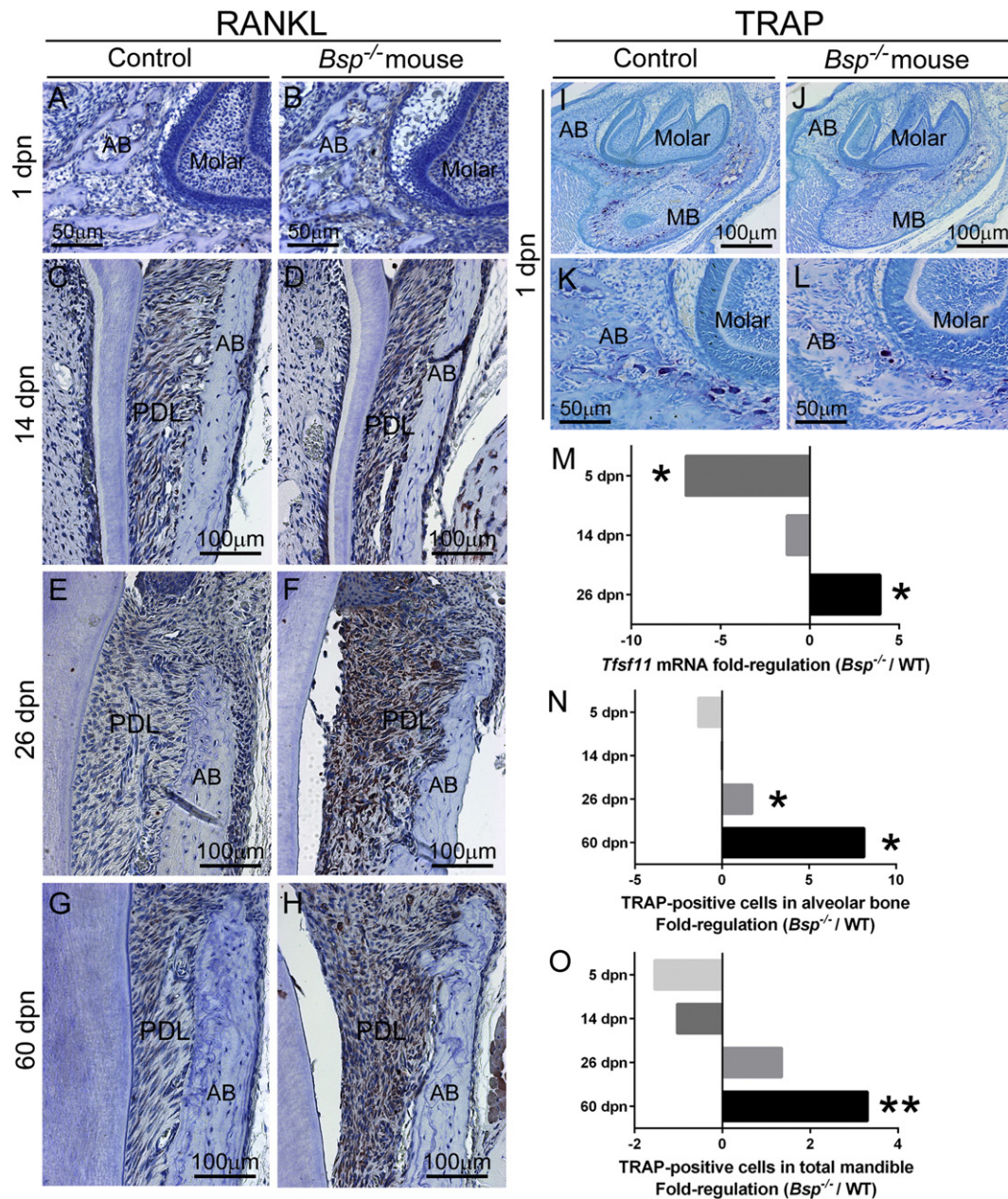


Fig. 5. Increased RANKL and osteoclastic cells in the functional alveolus of the *Bsp* null mouse. (A–H) IHC for RANKL identifies increased staining in *Bsp*^{-/-} versus WT mouse periodontal ligament (PDL) over time, accompanying increased resorption of the adjacent alveolar bone (AB). Increased RANKL in *Bsp*^{-/-} mice is most notable at (F) 26 dpn, the first age following functional occlusion, though levels remain elevated at (H) 60 dpn. (I–L) TRAP staining was performed on tissue over 5–60 dpn to analyze osteoclastic numbers (e.g., large purple multi-nucleated cells in panels I–L) in the alveolar bone and mandibular bone (MB). Representative TRAP staining from 5 dpn tissues is shown in panels I–L. (M) Quantitative PCR revealed significantly reduced *Tnfsf11* (*Rankl*) mRNA ($p < 0.05$) in *Bsp*^{-/-} versus WT PDL at early age, and 5-fold significantly increased ($p < 0.05$) *Tnfsf11* in *Bsp*^{-/-} mouse PDL by 60 dpn. The number of TRAP-positive osteoclasts also increased in (N) alveolar bone and (O) total (alveolar and mandibular) bone in *Bsp*^{-/-} mice versus WT at later ages, where * indicates significant intergroup difference ($p < 0.05$) by independent samples *t*-test, and ** indicates $p < 0.01$ ($n = 3$ –7 samples per genotype at all ages).

dentin from natively mineralized tissue revealed no significant differences in collagen–mineral organization in *Bsp*^{-/-} compared to WT mice (Figs. 6N and P). In both cases, electron diffraction patterns showed arcs consistent with (002) plane of hydroxyapatite, showing preferential orientation along the long axis of the collagen fibrils. In addition, regions of banding are evident in both micrographs, indicative of preferential deposition of mineral into the gap region of the collagen fibrils, as is characteristic of mineralized connective tissues. Taken together, these results suggest that the mineralization of collagen fibrils in dentin is not significantly affected at the ultrastructural level by the deletion of BSP.

Odontoblast markers were assayed by IHC, including OSX, TNAP, osteocalcin (OCN), and dentin sialoprotein (DSP). No alterations in timing or localization of protein expression were noted during crown (1 dpn) or root (14 dpn) dentinogenesis (Supplementary Fig. 4).

Effect of loss of BSP on endochondral bone formation and craniofacial shape

Alterations in the epiphyseal growth plate of *Bsp*^{-/-} mice have been reported at early ages, as well as low bone formation rate [12,40]. However, neither frank osteomalacia nor accumulation of osteoid on cortical or trabecular bone surfaces have been identified (Figs. 7A–D

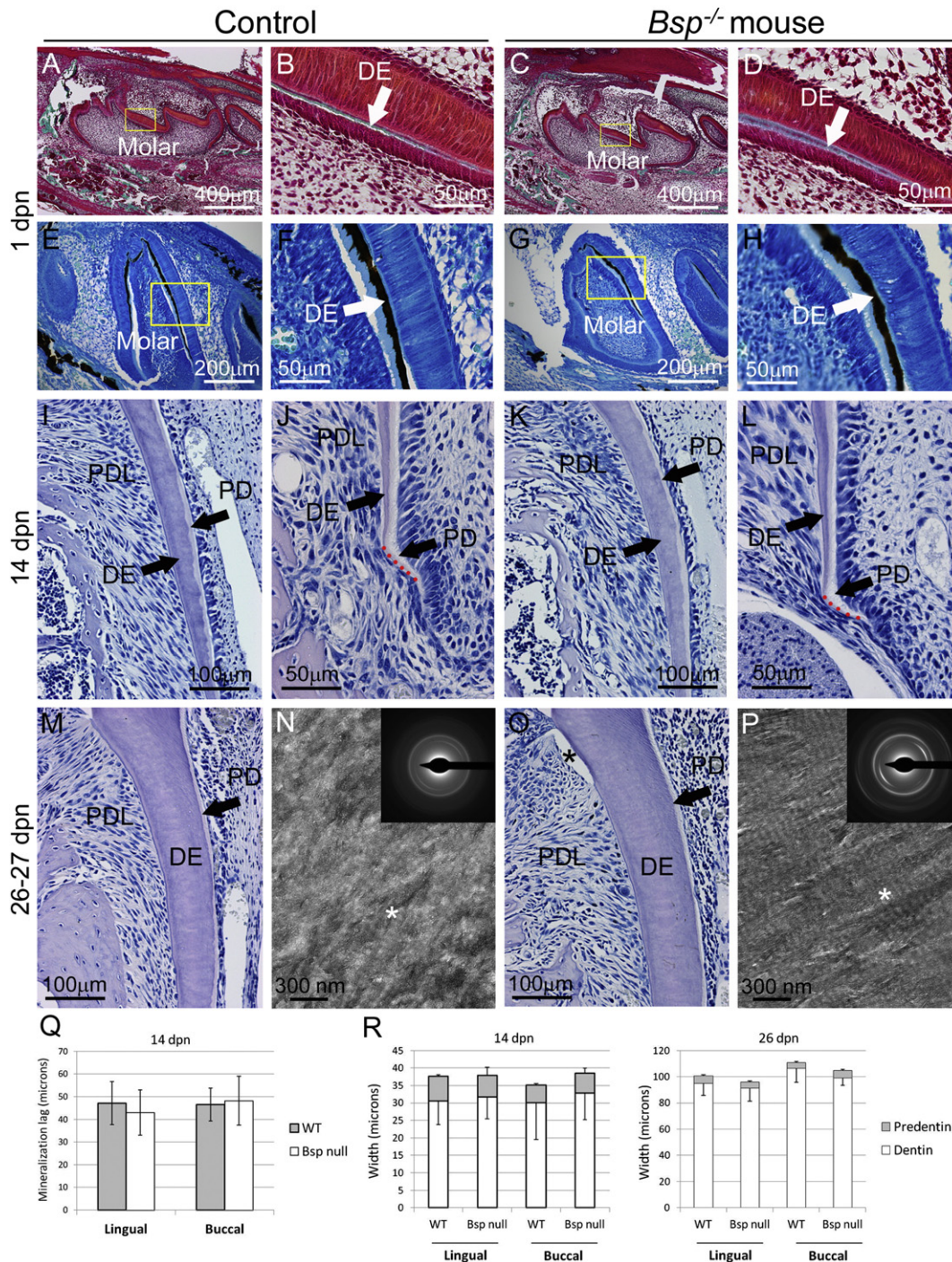


Fig. 6. Loss of BSP does not affect molar dentin formation or mineralization. Compared to controls, initiation of dentin (DE) mineralization is not delayed in *Bsp*^{-/-} mouse molars by (A–D) Goldner’s trichrome staining or (E–H) von Kossa staining, of undecalcified sections at 1 dpn. Yellow boxes in panels A, C, E, and G indicate areas shown under higher magnification in panels B, D, F, and H, respectively. The lag in mineralization between predentin (PD) matrix secretion (pale, whitish) and mineralization to dentin proper (light pink-purple) at the apical root tip is not delayed in *Bsp*^{-/-} mice compared to control (J vs. L, and Q). No differences in the widths of root dentin and predentin at (I, K) 14 dpn or (M, O) 26 dpn in *Bsp*^{-/-} vs. WT are observed, as confirmed by statistical analysis in panel R (n = 4–6 samples per genotype for all ages). (N, P) TEM micrographs of unstained, natively mineralized dentin sections from 27 dpn mice show normal characteristics in both WT and *Bsp*^{-/-} litter mates. In both micrographs, regions of collagen banding are evident (asterisk), indicating preferential gap zone mineral deposition. Electron diffraction (insets) in both WT and *Bsp*^{-/-} molars show oriented arcs indicating preferential alignment of the hydroxyapatite (002) plane with the collagen fibril axis.

and [12,58]). We examined the effect of loss of BSP on cranial endochondral ossification by analyzing the growth plates of the spheno-occipital synchondrosis (SOS) and the pre-sphenoidal synchondrosis (PSS).

The growth plates of the PSS and SOS were visible in WT and *Bsp*^{-/-} mice at 1 dpn (Figs. 7E–H). Alcian blue/nuclear fast red and safranin-O/fast green stains, differential for cartilage due to the high content of

polyanionic proteoglycans, revealed normal overall structures for PSS and SOS in WT and *Bsp*^{-/-} mice (Figs. 7I–L). Further analyses using von Kossa and Goldner trichrome stains indicated mineralized cartilage in growth plates, and mineralized cortical and trabecular bone in both WT and *Bsp*^{-/-} mice (Figs. 7M–P). No differences were noted in growth plate morphology or onset of mineralization in *Bsp*^{-/-} versus WT mice.

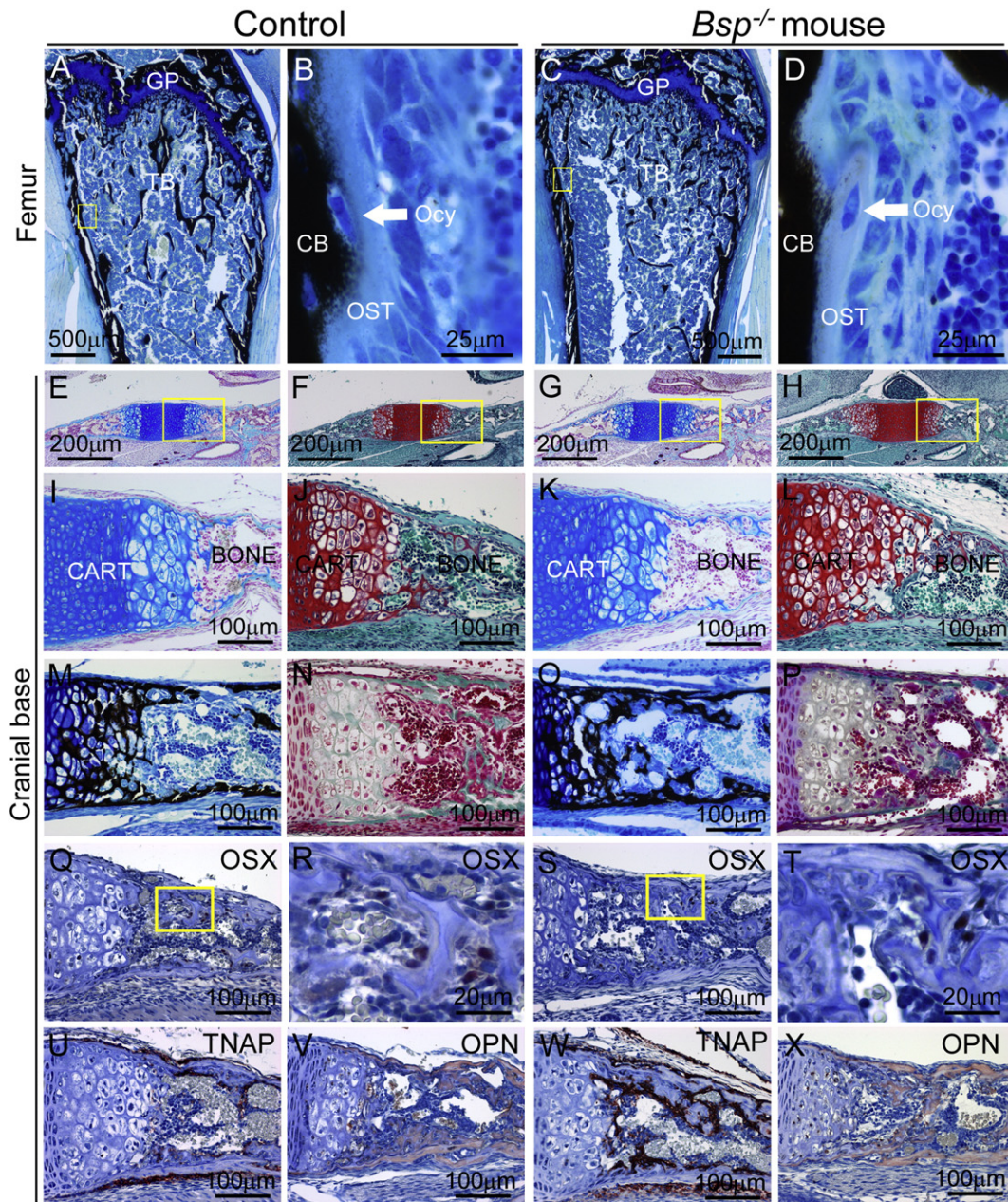


Fig. 7. Effect of loss of BSP on endochondral ossification in the cranial base. (A, B) At 1 mo, femurs of *Bsp*^{-/-} mice have grossly normal morphology of the growth plate (GP), with increased trabecular bone (TB). High magnification of von Kossa stained sections shows no substantial accumulation of osteoid (OST) in the conversion to mineralized cortical bone (CB), a process in which osteocytes (Ocy) are embedded. Yellow boxes in panels A and C indicate areas shown under higher magnification in panels B and D, respectively. The remaining panels (E–V) feature the cranial base synchondrosis at 1 dpn, where yellow boxes in row E–H indicate areas shown under higher magnification in row I–L. Histological stains for cartilage, including alcian blue/nuclear fast red (E, I, G, K) and safranin-O (F, H, J, L) reveal no morphological differences in the cranial base cartilage between *Bsp*^{-/-} and WT mice. Stains for mineralization status, including von Kossa (M, O) and Goldner's trichrome (N, P) do not reveal any substantial mineralization defects in *Bsp*^{-/-} versus WT mice. In cranial base, no differences in early (Q–T) osteoblast marker osterix (OSX) expression are observed in *Bsp* null versus WT. Yellow boxes in panels Q and S indicate areas shown under higher magnification in panels R and T, respectively. (U, W) Tissue nonspecific alkaline phosphatase (TNAP) localization appears increased in *Bsp* null endochondral bone compared to WT. (V, X) Osteopontin (OPN) is present in endochondral bone matrix in WT and *Bsp*^{-/-} mice.

In long bones, while chondrocyte markers were not altered by loss of BSP, changes in several osteoblast markers were noted [12,40]. Osteoblast markers were assayed in PSS and SOS bone by IHC, including OSX, TNAP, and OPN. Expression and localization of OSX was similar in WT and *Bsp*^{-/-} bone (Figs. 7Q–T). As with alveolar and mandibular bone (Fig. 3), TNAP appeared to be increased in *Bsp*^{-/-} versus WT mice around new bone of the cranial base (Figs. 7U and W). No differences were detected for OPN localization in cortical or endochondral bone matrix (Figs. 7V and X).

Growth plates of the cranial base contribute to elongation of the neurocranium and midfacial growth. Substantial alterations in

endochondral ossification in the cranial base would thus be expected to have consequences in terms of midfacial growth, and this has been borne out in transgenic and knock-out mouse models ablating factors essential for regulating endochondral bone growth and mineralization [7,53,64,84]. We performed a quantitative comparison of craniofacial parameters in WT and *Bsp*^{-/-} crania to determine if cranial morphology was altered by loss of BSP. Significant differences were not found between crania of WT and *Bsp*^{-/-} mice in skull length, nose length, nasal bone length, frontal bone length, parietal bone length, upper jaw length, premaxilla width, lacrimal width, squamosal width, skull width, or skull height (Supplementary Table 2). While *Bsp*^{-/-} mouse

crania trended towards decreased size in several parameters at 5 dpn, this was not generally the case at 14 dpn, with skull width of *Bsp*^{-/-} mice being increased. By 26 dpn, all cranial measurements trended towards increase in *Bsp*^{-/-} versus WT mice ($p > 0.05$), matching patterns of reversal observed in parietal bone microCT analysis and suture measurements (Supplemental Table 1 and Table 1), and consistent with effects from reduced osteoclast activity with the loss of BSP [58, 83]. The absence of large changes in craniofacial size and shape supports histological observations that the cranial base forms and mineralizes normally in *Bsp*^{-/-} mice.

Discussion

BSP is a multifunctional protein associated with the ECM of mineralized tissues, hypothesized to function in cell differentiation and mineralization. We analyzed how loss of BSP affected development, differentiation, and maturation of the craniofacial region in *Bsp*^{-/-} mice, focusing on bone, dental cementum, and dentin. Intramembranous bone at several sites in *Bsp*^{-/-} mouse crania exhibited delayed mineralization, with most severe effects observed in the alveolar bone and mandible. Tooth root acellular cementum failed to form in the absence of BSP, leading to poor anchorage of PDL Sharpey's fibers and structural defects at the root surface, though the PDL–bone interface appeared unaffected. Increasing RANKL expression and osteoclast numbers in *Bsp*^{-/-} mouse mandibles and alveolar bone were observed following molar tooth eruption, suggesting a role for tooth dysfunction and/or occlusal trauma in the bone loss and periodontal destruction with advanced ages. In contrast, dentin formation and mineralization was normal in *Bsp* null molar teeth. Unlike sites of intramembranous ossification, endochondral bone formation of the cranial base appeared normal and craniofacial morphology was unaffected in *Bsp*^{-/-} mice. Most significantly, these collected data show that functional importance for BSP is site-specific, with the most dramatic effects from loss of BSP on mineralization of cementum and alveolar bone, ultimately causing periodontal dysfunction and breakdown.

Functional importance of BSP in intramembranous osteogenesis and periodontal function

The mandible, alveolus, and some bones of the calvaria arise from neural crest and form by intramembranous ossification, where nodules of osteoprogenitor cells secrete collagenous extracellular matrix (osteoid) that is subsequently mineralized, with no cartilage anlage [14,65]. BSP is present at early time points in the matrices of these tissues (as in Fig. 1) [16,17,26,56,57,61]. At all sites of intramembranous ossification analyzed, including sutures of the cranium, and in mandibular and alveolar bone, *Bsp*^{-/-} mice featured delayed mineralization compared to WT. Extensive regions of osteoid accumulation were especially pronounced in *Bsp*^{-/-} mouse mandibular and alveolar bone at early ages, supporting an important role for BSP in early matrix mineralization. Alveolar and mandibular bone, as well as tooth root cementum, were analyzed to define the functional importance of BSP in those tissues.

Alveolar bone and cementum are components of the periodontal attachment apparatus, separated by the unmineralized PDL. BSP is present in the ECM of cementum and alveolar bone of the periodontal support apparatus (Fig. 1 and [10,26,28,56,57,61]). During development, collagen fibers of the PDL insert into both the cementum and bone surfaces. Upon entering occlusion, these embedded Sharpey's fibers provide attachment, while accommodating the loads that accompany tooth use [38,39]. Using SEM and TEM, we confirmed the absence of acellular cementum on tooth root surfaces of *Bsp*^{-/-} mice, as well as poorly embedded Sharpey's fibers, and detachment and disorganization of collagen fibrils (Fig. 4). In contrast, at the PDL–bone interface, Sharpey's fibers insertion appeared unaffected and detachment was not observed.

These observations provide insight into the role of BSP in these tissues, and likely reflect differences in their modes of formation. Intramembranous bone forms as a two-step process whereby osteoblasts secrete the ECM (osteoid), and then in a second step, the matrix becomes mineralized in a regulated process. In contrast, acellular cementum formation involves a directed mineralization of the collagen fringe fibers at the tooth root surface [9], a process that we and others have found to be heavily reliant on the physicochemical process of mineralization [4,5,22,24,45,47,62,66,88]. With lack of BSP, craniofacial intramembranous bone is delayed in the conversion from osteoid to mineralized bone. However, bone matrix formation appears normal, including insertion of Sharpey's fibers at the PDL–alveolar bone interface, and we hypothesize that bone remodeling over time allows for adaptation and functionality despite early hypomineralization (though insertion into bone may be relatively weakened). Additionally, while some alterations in osteoblast marker genes have been identified in *Bsp*^{-/-} mice long bones [40,58] and calvarial bones (this paper), we did not identify significant differences in *OSX*, *TNAP*, or *OPN* in alveolar and mandibular bone by IHC or PCR (at 1 and 5 dpn, respectively). The increased *TNAP* immunostaining observed in craniofacial and alveolar bone mirrors increased circulating ALP activity reported previously [26], and we hypothesize this is a compensatory mechanism related to defects in skeletal formation and mineralization in *Bsp*^{-/-} mice.

These data support the concept that lack of BSP most severely affects the matrix mineralization phase in intramembranous bone, indicating a direct role for BSP in HA crystal formation or growth. Acellular cementum is inhibited from forming in *Bsp*^{-/-} mice, and we hypothesize that lack of matrix mineralization also underlies this defect. In the case of acellular cementum, the sensitivity to mineralization disturbances and lack of physiological remodeling create a scenario where there is a narrow developmental window for the cementum layer to form and subsequently, properly anchor Sharpey's fibers. In the absence of functional cementum, the PDL–tooth interface is compromised as soon as the tooth enters occlusion, and PDL attachment and tooth function are lost. Studies underway to define effects of *Ibsp* knock-out on cementoblast differentiation and function will provide additional insights on role(s) of BSP in regulating mineralization versus potential roles in cell signaling. The importance of BSP for cementum and alveolar bone mineralization and periodontal function identify this as a molecule of interest for regenerative applications including periodontal disease, osteoporosis, and others.

A reduction in bone turnover in the postcranial skeleton has been documented in *Bsp*^{-/-} mice [58,83], and the role of BSP in supporting osteoclast differentiation has been shown [11,81]. There is a striking reversal in craniofacial parameters of *Bsp*^{-/-} mice versus controls, from younger to older ages. *Bsp*^{-/-} mice at 5 dpn feature decreased mineral properties of parietal bones, increased suture widths, and smaller cranial measurements (all suggesting delays in bone formation), whereas *Bsp*^{-/-} mice at 26 dpn exhibit increased mineral properties of parietal bones, decreased suture widths, and larger cranial measurements (all suggesting defects in bone remodeling, supported by decreased expression of osteoclast factors *Acp5/TRAP* and *Tnfrsf11a/RANK* in calvarial tissues). These observations are consistent with delayed bone formation, followed by defective osteoclast recruitment, as previously reported [11,58,82,83]. We analyzed mandibular and alveolar bone more closely. At early ages, we show low/normal numbers of osteoclasts in *Bsp* null mandibular and alveolar bone, compared to controls. However, increased numbers of osteoclasts were observed in *Bsp*^{-/-} mouse mandibles at later ages of 26 and 60 dpn, after the molar was erupted and in occlusion, and the lack of cementum has predisposed to PDL detachment. This temporal pattern suggests strongly that tooth and bone resorption and alveolar bone reduction, previously observed in *Bsp*^{-/-} mice at later ages [26], arise as a consequence of dysfunctional cementum and weakened ability to withstand mechanical forces arising from occlusion. We demonstrated that mRNA and protein for RANKL increases over time in the PDL of *Bsp*^{-/-} mice compared to

controls, providing a proximal mechanism for the increase in osteoclast numbers and incidence of bone and root resorption. In order to better understand the effect of occlusal forces on resorption observed in the mandibles of *Bsp*^{-/-} mice, we are currently determining the effects of hard versus soft diet on tooth formation and function.

BSP in dentin formation and potential for compensation

BSP is part of the SIBLING protein family, also including mineralized tissue-associated phosphoproteins OPN, DMP1, DSP, DPP, and MEPE [21,69,77]. The SIBLING family is part of a larger secretory calcium-binding phosphoprotein (SCPP) family clustered on mouse chromosome 5 (and human chromosome 4), predicted to have evolved from a common ancestor by gene duplication, and also including a group of enamel-selective proteins, and other secreted saliva and milk proteins [48–50]. These proteins have in common some genomic structural elements, as well as biochemical features considered critical for their functions as calcium-binding proteins, notably acidic amino acid motifs (e.g. glutamic acid and aspartic acid) and phosphorylated serine residues [69]. It has been speculated that because of biochemical similarities, some SCPP and SIBLING proteins may hold redundant functions or partially compensate in one another's absence, though some evidence (including in this paper) also points to specific and non-redundant functions.

Functional analysis of SCPP and SIBLING proteins has involved evolutionary, bioinformatics, in vitro cell assay, and in vivo approaches. Knock-out mouse approaches, in particular, provide evidence for not only overall functional importance, but can also pinpoint affected tissues and help identify compensatory mechanisms. Ablation of SCPP enamel-selective genes ameloblastin and enamelin result in severe defects in amelogenesis and enamel mineralization, indicating distinct and non-redundant functions [18,42,73]. Gene knock-out of each SIBLING member has affected skeletal and/or dental mineralization. *Spp1*^{-/-} mice featured increased skeletal bone mineral content and crystallinity, consistent with the proposed function of OPN as a negative regulator of mineralization [8]. Knock-out of *Mepe*/OF45 resulted in increased bone formation and mass [35], while over-expression inhibited long bone growth plate mineralization [76]. Knock-out of *Dmp1* revealed not only direct effects on dentin and bone [52,54], but a role in systemic phosphate homeostasis [20], while targeted ablation of *Dspp* primarily targets dentin and periodontal tissues [31,75].

We observed substantial mineralization defects in mandibular and alveolar bone and cementum stemming from loss of BSP, supporting an important and non-redundant role for BSP in those tissues. However, a detailed developmental study of dentinogenesis in the *Bsp*^{-/-} mouse revealed no observable defects in dentin formation, organization, mineralization, collagen-mineral ultrastructure, or in odontoblast marker profile. The presence and relative quantity of BSP in the dentin ECM has been a source of disagreement. BSP expression has been reported in odontoblasts, though relatively low expression has been observed in some studies [13,15,16]. BSP concentration in dentin has been reported to be one tenth that in bone [27], while another study estimated similar BSP concentrations in the two tissues [68]. The lack of dentin phenotype in the absence of BSP supports the interpretation that BSP has no critical and non-redundant function in mouse dentin formation.

Notably, circumpulpal dentin formation has been described as depending on other ECM proteins, including related SIBLING family members DMP1, DSP, and DPP [6,32,54,67,75,78,79,86]. Like BSP, these multifunctional SIBLINGs can both directly and indirectly affect mineralization, and may also be involved in cell signaling and differentiation, and other local or systemic effects [29,30,37,44,72,80]. Mutations in *DSPP* (the gene encoding DSP and DPP) cause dentin dysplasia and dentinogenesis imperfecta in humans [41,55], where dentin is thin and hypomineralized. While BSP appears to function in bone and cementum mineralization, other proteins may perform equivalent roles for dentinogenesis.

BSP in craniofacial endochondral ossification

In the femur, which arises from paraxial mesoderm and undergoes endochondral ossification, alterations in the epiphyseal growth plate and low rates of bone formation have been reported at early ages in *Bsp*^{-/-} mice [12,40]. Signs of osteomalacia have not been identified on cortical or trabecular bone surfaces (Figs. 7A–D and [12,58]). Portions of the neurocranium, the braincase that occupies the back portions of the skull, also arise from paraxial mesoderm and form through the process of endochondral ossification [65]. No defects were identified in bone forming by endochondral ossification in the cranial base due to the absence of BSP. The synchondroses examined appeared normal in structure and matrix content. There was no sign of frank delay in mineralization or osteoid accumulation in the associated bone, and bone markers appeared normally expressed. Moreover, craniofacial size and shape were not affected by loss of BSP (Supplementary Table 2), strongly suggesting no deleterious effects of loss of BSP on endochondral bone formation driving craniofacial growth.

While these differential effects are striking, it is difficult to say within the limitations of the study whether they arise from the method of ossification (intramembranous vs. endochondral), origin of bone cells (cranial neural crest ectomesenchyme or mesoderm), or whether the more severe mineralization defects are particular to the bone of the mandible and alveolus. We are currently generating an *Ibsp* floxed allele in order to better understand contributions of BSP to individual tissue compartments.

Conclusions

In summary, we report that loss of BSP affects mineralized tissues of the dental–oral–craniofacial complex differently, with severe effects to cementum and bones of the alveolus and mandible, and little or no effect on dentin or endochondral bone of the cranial base. Where defects in formation were noted, loss of BSP appears to most severely affect the process of mineralization, supporting an important and direct in vivo role for BSP in HA crystal deposition and/or growth. Increased resorption in the mandible in the absence of BSP is opposite to the low bone turnover in long bones and calvaria, and is likely a secondary effect from the breakdown in periodontal structure and function.

Supplementary data to this article can be found online at <http://dx.doi.org/10.1016/j.bone.2015.05.007>.

Acknowledgments

This research was supported by sources including grant AR 066110 to BLF from the National Institute of Arthritis and Musculoskeletal and Skin Diseases (NIAMS)/NIH, the Intramural Research Program of NIAMS (MJS), the Canadian Institutes of Health Research (#130572; HAG), and the CIHR Institute of Musculoskeletal Health and Arthritis (#134216; EDS). We thank Kenn Holmbeck of the National Institute of Dental and Craniofacial Research (NIDCR) for assistance with microCT analysis and Nasrin Kalantari Pour (NIAMS) for assistance with histology.

References

- [1] Baht GS, Hunter GK, Goldberg HA. Bone sialoprotein–collagen interaction promotes hydroxyapatite nucleation. *Matrix Biol* 2008;27(7):600–8.
- [2] Baht GS, O'Young J, Borovina A, Chen H, Tye CE, Karttunen M, et al. Phosphorylation of Ser136 is critical for potent bone sialoprotein-mediated nucleation of hydroxyapatite crystals. *Biochem J* 2010;428(3):385–95.
- [3] Beederman M, Farina EM, Reid RR. Molecular basis of cranial suture biology and disease: osteoblastic and osteoclastic perspectives. *Genes Dis* 2014;1(1):120–5.
- [4] Beertsen W, Niehof A, Everts V. Effects of 1-hydroxyethylidene-1, 1-bisphosphonate (HEBP) on the formation of dentin and the periodontal attachment apparatus in the mouse. *Am J Anat* 1985;174(1):83–103.
- [5] Beertsen W, VandenBos T, Everts V. Root development in mice lacking functional tissue non-specific alkaline phosphatase gene: inhibition of acellular cementum formation. *J Dent Res* 1999;78(6):1221–9.

- [6] Bleicher F, Couble M, Farges J, Couble P, Magloire H. Sequential expression of matrix protein genes in developing rat teeth. *Matrix Biol* 1999;18(2):133–43.
- [7] Bloom MW, Murakami S, Cody D, Montufar-Solis D, Duke PJ. Aspects of achondroplasia in the skulls of dwarf transgenic mice: a cephalometric study. *Anat Rec A Discov Mol Cell Evol Biol* 2006;288(3):316–22.
- [8] Boskey AL, Spevak L, Paschalis E, Doty SB, McKee MD. Osteopontin deficiency increases mineral content and mineral crystallinity in mouse bone. *Calcif Tissue Int* 2002;71(2):145–54.
- [9] Bosshardt D, Schroeder H. Establishment of acellular extrinsic fiber cementum on human teeth. A light- and electron-microscopic study. *Cell Tissue Res* 1991;263(2):325–36.
- [10] Bosshardt D, Zalzal S, McKee M, Nanci A. Developmental appearance and distribution of bone sialoprotein and osteopontin in human and rat cementum. *Anat Rec* 1998;250(1):13–33.
- [11] Boudiffa M, Wade-Gueye NM, Guignandon A, Vanden-Bossche A, Sabido O, Aubin JE, et al. Bone sialoprotein deficiency impairs osteoclastogenesis and mineral resorption in vitro. *J Bone Miner Res* 2010;25(12):2669–79.
- [12] Boulefour W, Boudiffa M, Wade-Gueye NM, Bouet G, Cardelli M, Laroche N, et al. Skeletal development of mice lacking bone sialoprotein (BSP) – impairment of long bone growth and progressive establishment of high trabecular bone mass. *PLoS One* 2014;9(5):e95144.
- [13] Butler W, Ritchie H. The nature and functional significance of dentin extracellular matrix proteins. *Int J Dev Biol* 1995;39(1):169–79.
- [14] Chai Y, Jiang X, Ito Y, Bringas PJ, Han J, Rowitch D, et al. Fate of the mammalian cranial neural crest during tooth and mandibular morphogenesis. *Development* 2000;127(8):1671–9.
- [15] Chen J, Shapiro H, Sodek J. Development expression of bone sialoprotein mRNA in rat mineralized connective tissues. *J Bone Miner Res* 1992;7(8):987–97.
- [16] Chen J, McCulloch CA, Sodek J. Bone sialoprotein in developing porcine dental tissues: cellular expression and comparison of tissue localization with osteopontin and osteonectin. *Arch Oral Biol* 1993;38(3):241–9.
- [17] Chen J, McKee MD, Nanci A, Sodek J. Bone sialoprotein mRNA expression and ultrastructural localization in fetal porcine calvarial bone: comparisons with osteopontin. *Histochem J* 1994;26(1):67–78.
- [18] Chun YH, Lu Y, Hu Y, Krebsbach PH, Yamada Y, Hu JC, et al. Transgenic rescue of enamel phenotype in *Ambn* null mice. *J Dent Res* 2010;89(12):1414–20.
- [19] D'Errico J, MacNeil R, Takata T, Berry J, Strayhorn C, Somerman M. Expression of bone associated markers by tooth root lining cells, in situ and in vitro. *Bone* 1997;20(2):117–26.
- [20] Feng JQ, Ward LM, Liu S, Lu Y, Xie Y, Yuan B, et al. Loss of DMP1 causes rickets and osteomalacia and identifies a role for osteocytes in mineral metabolism. *Nat Genet* 2006;38(11):1310–5.
- [21] Fisher LW, Fedarko NS. Six genes expressed in bones and teeth encode the current members of the SIBLING family of proteins. *Connect Tissue Res* 2003;44(Suppl. 1):33–40.
- [22] Foster BL, Nagatomo KJ, Bamashmous SO, Tompkins KA, Fong H, Dunn D, et al. The progressive ankylosis protein regulates cementum apposition and extracellular matrix composition. *Cells Tissues Organs* 2011;194(5):382–405.
- [23] Foster BL. Methods for studying tooth root cementum by light microscopy. *Int J Oral Sci* 2012;4(3):119–28.
- [24] Foster BL, Nagatomo KJ, Nociti FH, Fong H, Dunn D, Tran AB, et al. Central role of pyrophosphate in acellular cementum formation. *PLoS One* 2012;7(6):e38393.
- [25] Foster BL, Nagatomo KJ, Tso HW, Tran AB, Nociti Jr FH, Narisawa S, et al. Tooth root dentin mineralization defects in a mouse model of hypophosphatasia. *J Bone Miner Res* 2013;28(2):271–82.
- [26] Foster BL, Soenjaya Y, Nociti FH, Holm E, Zerfas PM, Wimer HF, et al. Deficiency in acellular cementum and periodontal attachment in *bsp* null mice. *J Dent Res* 2013;92(2):166–72.
- [27] Fujisawa R, Butler WT, Brunn JC, Zhou HY, Kuboki Y. Differences in composition of cell-attachment sialoproteins between dentin and bone. *J Dent Res* 1993;72(8):1222–6.
- [28] Ganss B, Kim R, Sodek J. Bone sialoprotein. *Crit Rev Oral Biol Med* 1999;10(1):79–98.
- [29] Gericke A, Qin C, Sun Y, Redfern R, Redfern D, Fujimoto Y, et al. Different forms of DMP1 play distinct roles in mineralization. *J Dent Res* 2010;89(4):355–9.
- [30] Gibson MP, Liu Q, Zhu Q, Lu Y, Jani P, Wang X, et al. Role of the NH2-terminal fragment of dentin sialophosphoprotein in dentinogenesis. *Eur J Oral Sci* 2013;121(2):76–85.
- [31] Gibson MP, Zhu Q, Liu Q, D'Souza RN, Feng JQ, Qin C. Loss of dentin sialophosphoprotein leads to periodontal diseases in mice. *J Periodontol Res* 2013;48(2):221–7.
- [32] Gibson MP, Zhu Q, Wang S, Liu Q, Liu Y, Wang X, et al. The rescue of dentin matrix protein 1 (DMP1)-deficient tooth defects by the transgenic expression of dentin sialophosphoprotein (DSPP) indicates that DSPP is a downstream effector molecule of DMP1 in dentinogenesis. *J Biol Chem* 2013;288(10):7204–14.
- [33] Goldberg HA, Hunter GK. Functional domains of bone sialoprotein. In: Goldberg M, editor. *Phosphorylated extracellular matrix proteins of bone and dentin*. Bentham Science Publishers; 2012. p. 266–82.
- [34] Gordon JA, Tye CE, Sampaio AV, Underhill TM, Hunter GK, Goldberg HA. Bone sialoprotein expression enhances osteoblast differentiation and matrix mineralization in vitro. *Bone* 2007;41(3):462–73.
- [35] Gowen LC, Petersen DN, Mansolf AL, Qi H, Stock JL, Tkalecic GT, et al. Targeted disruption of the osteoblast/osteocyte factor 45 gene (OF45) results in increased bone formation and bone mass. *J Biol Chem* 2003;278(3):1998–2007.
- [36] Hatch NE. FGF signaling in craniofacial biological control and pathological craniofacial development. *Crit Rev Eukaryot Gene Expr* 2010;20(4):295–311.
- [37] He G, Dahl T, Veis A, George A. Dentin matrix protein 1 initiates hydroxyapatite formation in vitro. *Connect Tissue Res* 2003;44(Suppl. 1):240–5.
- [38] Herber RP, Fong J, Lucas SA, Ho SP. Imaging an adapted dentoalveolar complex. *Anat Res Int* 2012;782571.
- [39] Ho S, Kurylo M, Fong T, Lee S, Wagner H, Ryder M, et al. The biomechanical characteristics of the bone–periodontal ligament–cementum complex. *Biomaterials* 2010;31(25):6635–46.
- [40] Holm E, Aubin JE, Hunter GK, Beier F, Goldberg HA. Loss of bone sialoprotein leads to impaired endochondral bone development and mineralization. *Bone* 2015;71:145–54.
- [41] Hu J, Simmer J. Developmental biology and genetics of dental malformations. *Orthod Craniofac Res* 2007;10(2):45–52.
- [42] Hu JC, Hu Y, Smith CE, McKee MD, Wright JT, Yamakoshi Y, et al. Enamel defects and ameloblast-specific expression in *Enam* knock-out/*lacZ* knock-in mice. *J Biol Chem* 2008;283(16):10858–71.
- [43] Huang B, Sun Y, Maciejewska I, Qin D, Peng T, McIntyre B, et al. Distribution of SIBLING proteins in the organic and inorganic phases of rat dentin and bone. *Eur J Oral Sci* 2008;116(2):104–12.
- [44] Hunter GK, Hauschka PV, Poole AR, Rosenberg LC, Goldberg HA. Nucleation and inhibition of hydroxyapatite formation by mineralized tissue proteins. *Biochem J* 1996;317(Pt 1):59–64.
- [45] Jayawardena C, Takahashi N, Watanabe E, Takano Y. On the origin of intrinsic matrix of acellular extrinsic fiber cementum: studies on growing cementum pearls of normal and bisphosphonate-affected guinea pig molars. *Eur J Oral Sci* 2002;110(3):261–9.
- [46] Kacena MA, Troiano NW, Wilson KM, Coady CE, Horowitz MC. Evaluation of two different methylmethacrylate processing, infiltration, and embedding techniques on the histological, histochemical, and immunohistochemical analysis of murine bone samples. *J Histotechnol* 2004;27(2):119–30.
- [47] Kaipatur N, Murshed M, McKee M. Matrix Gla protein inhibition of tooth mineralization. *J Dent Res* 2008;87(9):839–44.
- [48] Kawasaki K, Suzuki T, Weiss KM. Genetic basis for the evolution of vertebrate mineralized tissue. *Proc Natl Acad Sci U S A* 2004;101(31):11356–61.
- [49] Kawasaki K, Buchanan AV, Weiss KM. Gene duplication and the evolution of vertebrate skeletal mineralization. *Cells Tissues Organs* 2007;186(1):7–24.
- [50] Kawasaki K, Weiss KM. SCPP gene evolution and the dental mineralization continuum. *J Dent Res* 2008;87(6):520–31.
- [51] Lee JC, Spiguel L, Shenaq DS, Zhong M, Wietholt C, He TC, et al. Role of RANK–RANKL–OPG axis in cranial suture homeostasis. *J Craniofac Surg* 2011;22(2):699–705.
- [52] Ling Y, Rios H, Myers E, Lu Y, Feng J, Boskey A. DMP1 depletion decreases bone mineralization in vivo: an FTIR imaging analysis. *J Bone Miner Res* 2005;20(12):2169–77.
- [53] Liu J, Nam HK, Campbell C, Gasque KC, Millan JL, Hatch NE. Tissue-nonspecific alkaline phosphatase deficiency causes abnormal craniofacial bone development in the *Alpl*($-/-$) mouse model of infantile hypophosphatasia. *Bone* 2014;67:81–94.
- [54] Lu Y, Ye L, Yu S, Zhang S, Xie Y, McKee M, et al. Rescue of odontogenesis in *Dmp1*-deficient mice by targeted re-expression of DMP1 reveals roles for DMP1 in early odontogenesis and dentin apposition in vivo. *Dev Biol* 2007;303(1):191–201.
- [55] MacDougall M, Dong J, Acevedo A. Molecular basis of human dentin diseases. *Am J Med Genet A* 2006;140(23):2536–46.
- [56] Macneil R, Sheng N, Strayhorn C, Fisher L, Somerman M. Bone sialoprotein is localized to the root surface during cementogenesis. *J Bone Miner Res* 1994;9(10):1597–606.
- [57] MacNeil R, Berry J, D'Errico J, Strayhorn C, Piotrowski B, Somerman M. Role of two mineral-associated adhesion molecules, osteopontin and bone sialoprotein, during cementogenesis. *Connect Tissue Res* 1995;33(1–3):1–7.
- [58] Malaval L, Wade-Gu ye NM, Boudiffa M, Fei J, Zirngibl R, Chen F, et al. Bone sialoprotein plays a functional role in bone formation and osteoclastogenesis. *J Exp Med* 2008;205(5):1145–53.
- [59] Malaval L, Aubin JE, Vico L. Role of the small integrin-binding ligand N-linked glycoprotein (SIBLING), bone sialoprotein (BSP) in bone development and remodeling. *Osteoporos Int* 2009;20(6):1077–80.
- [60] Malaval L, Monfoulet L, Fabre T, Pothuaud L, Bareille R, Miroux S, et al. Absence of bone sialoprotein (BSP) impairs cortical defect repair in mouse long bone. *Bone* 2009;45(5):853–61.
- [61] McKee M, Zalzal S, Nanci A. Extracellular matrix in tooth cementum and mantle dentin: localization of osteopontin and other noncollagenous proteins, plasma proteins, and glycoconjugates by electron microscopy. *Anat Rec* 1996;245(2):293–312.
- [62] McKee MD, Nakano Y, Masica DL, Gray JJ, Lemire I, Heft R, et al. Enzyme replacement therapy prevents dental defects in a model of hypophosphatasia. *J Dent Res* 2011;90(4):470–6.
- [63] Monfoulet L, Malaval L, Aubin JE, Rittling SR, Gadeau AP, Fricain JC, et al. Bone sialoprotein, but not osteopontin, deficiency impairs the mineralization of regenerating bone during cortical defect healing. *Bone* 2010;46(2):447–52.
- [64] Nakao K, Okubo Y, Yasoda A, Koyama N, Osawa K, Isobe Y, et al. The effects of C-type natriuretic peptide on craniofacial skeletogenesis. *J Dent Res* 2013;92(1):58–64.
- [65] Nanci A. *Ten Cate's oral histology: development, structure, and function*. 8th ed. St. Louis, MO: Elsevier; 2012.
- [66] Nociti FJ, Berry J, Foster B, Gurley K, Kingsley D, Takata T, et al. Cementum: a phosphate-sensitive tissue. *J Dent Res* 2002;81(12):817–21.
- [67] Ohma N, Takagi Y, Takano Y. Distribution of non-collagenous dentin matrix proteins and proteoglycans, and their relation to calcium accumulation in bisphosphonate-affected rat incisors. *Eur J Oral Sci* 2000;108(3):222–32.
- [68] Qin C, Brunn J, Jones J, George A, Ramachandran A, Gorski J, et al. A comparative study of sialic acid-rich proteins in rat bone and dentin. *Eur J Oral Sci* 2001;109(2):133–41.

- [69] Qin C, Baba O, Butler W. Post-translational modifications of sibling proteins and their roles in osteogenesis and dentinogenesis. *Crit Rev Oral Biol Med* 2004;15(3):126–36.
- [70] Rice D, Rice R, Thesleff I. Molecular mechanisms in calvarial bone and suture development, and their relation to craniosynostosis. *Eur J Orthod* 2003;25(2):139–48.
- [71] Richtsmeier JT, Baxter LL, Reeves RH. Parallels of craniofacial maldevelopment in Down syndrome and Ts65Dn mice. *Dev Dyn* 2000;217(2):137–45.
- [72] Siyam A, Wang S, Qin C, Mues G, Stevens R, D'Souza RN, et al. Nuclear localization of DMP1 proteins suggests a role in intracellular signaling. *Biochem Biophys Res Commun* 2012;424(3):641–6.
- [73] Smith CE, Wazen R, Hu Y, Zalzal SF, Nanci A, Simmer JP, et al. Consequences for enamel development and mineralization resulting from loss of function of ameloblastin or enamelin. *Eur J Oral Sci* 2009;117(5):485–97.
- [74] Somerman M, Shroff B, Agraves W, Morrison G, Craig A, Denhardt D, et al. Expression of attachment proteins during cementogenesis. *J Biol Buccale* 1990;18(3):207–14.
- [75] Sreenath T, Thyagarajan T, Hall B, Longenecker G, D'Souza R, Hong S, et al. Dentin sialophosphoprotein knockout mouse teeth display widened predentin zone and develop defective dentin mineralization similar to human dentinogenesis imperfecta type III. *J Biol Chem* 2003;278(27):24874–80.
- [76] Staines KA, Mackenzie NC, Clarkin CE, Zelenchuk L, Rowe PS, MacRae VE, et al. MEPE is a novel regulator of growth plate cartilage mineralization. *Bone* 2012;51(3):418–30.
- [77] Staines KA, MacRae VE, Farquharson C. The importance of the SIBLING family of proteins on skeletal mineralisation and bone remodelling. *J Endocrinol* 2012;214(3):241–55.
- [78] Steinfort J, van den Bos T, Beertsen W. Differences between enamel-related and cementum-related dentin in the rat incisor with special emphasis on the phosphoproteins. *J Biol Chem* 1989;264(5):2840–5.
- [79] Steinfort J, Beertsen W, van den Bos T. The possible relationship between the mineralization of dentin and the composition of its organic matrix. *J Biol Buccale* 1990;18(2):131–3.
- [80] Tartaix P, Doulaverakis M, George A, Fisher L, Butler W, Qin C, et al. In vitro effects of dentin matrix protein-1 on hydroxyapatite formation provide insights into in vivo functions. *J Biol Chem* 2004;279(18):18115–20.
- [81] Valverde P, Tu Q, Chen J. BSP and RANKL induce osteoclastogenesis and bone resorption synergistically. *J Bone Miner Res* 2005;20(9):1669–79.
- [82] Wade-Gueye NM, Boudiffa M, Laroche N, Vanden-Bossche A, Fournier C, Aubin JE, et al. Mice lacking bone sialoprotein (BSP) lose bone after ovariectomy and display skeletal site-specific response to intermittent PTH treatment. *Endocrinology* 2010;151(11):5103–13.
- [83] Wade-Gueye NM, Boudiffa M, Vanden-Bossche A, Laroche N, Aubin JE, Vico L, et al. Absence of bone sialoprotein (BSP) impairs primary bone formation and resorption: the marrow ablation model under PTH challenge. *Bone* 2012;50(5):1064–73.
- [84] Wang Y, Spatz MK, Kannan K, Hayk H, Avivi A, Gorivodsky M, et al. A mouse model for achondroplasia produced by targeting fibroblast growth factor receptor 3. *Proc Natl Acad Sci U S A* 1999;96(8):4455–60.
- [85] Wazen RM, Tye CE, Goldberg HA, Hunter GK, Smith CE, Nanci A. In vivo functional analysis of polyglutamic acid domains in recombinant bone sialoprotein. *J Histochem Cytochem* 2007;55(1):35–42.
- [86] Ye L, MacDougall M, Zhang S, Xie Y, Zhang J, Li Z, et al. Deletion of dentin matrix protein-1 leads to a partial failure of maturation of predentin into dentin, hypomineralization, and expanded cavities of pulp and root canal during postnatal tooth development. *J Biol Chem* 2004;279(18):19141–8.
- [87] Zhao H, Feng J, Ho TV, Grimes W, Urata M, Chai Y. The suture provides a niche for mesenchymal stem cells of craniofacial bones. *Nat Cell Biol* 2015;17(4):386–96.
- [88] Zweifler LE, Patel MK, Nociti Jr FH, Wimer HF, Millan JL, Somerman MJ, et al. Counter-regulatory phosphatases TNAP and NPP1 temporally regulate tooth root cementogenesis. *Int J Oral Sci* 2014;7(1):27–41.

Supplementary Table 1. MicroCT analysis of parietal bones. Parietal bone analyses were compared in WT and *Bsp*^{-/-} mice at 5, 14, and 26 dpn (n=4-5 for each genotype and age). After 3D reconstruction, volumes of parietal bone were contoured and segmented using a global threshold 0.25 g HA/cm³. Values are reported as mean ± SD.

	5 dpn		14 dpn		26 dpn	
	WT	<i>Bsp</i> ^{-/-}	WT	<i>Bsp</i> ^{-/-}	WT	<i>Bsp</i> ^{-/-}
Bone Thickness (µm)	26 ± 2	26 ± 2	38 ± 2	42 ± 2 *	71.2 ± 7.8	90.5 ± 4.2**
BV/TV (%)	22.34 ± 5.71	22.97 ± 3.47	43.74 ± 5.25	49.13 ± 3.07	78.27 ± 2.62	84.09 ± 0.60**
TMD (mg HA/cm³)	461 ± 23	461 ± 6	490 ± 13	482 ± 7	582 ± 24	618 ± 15*

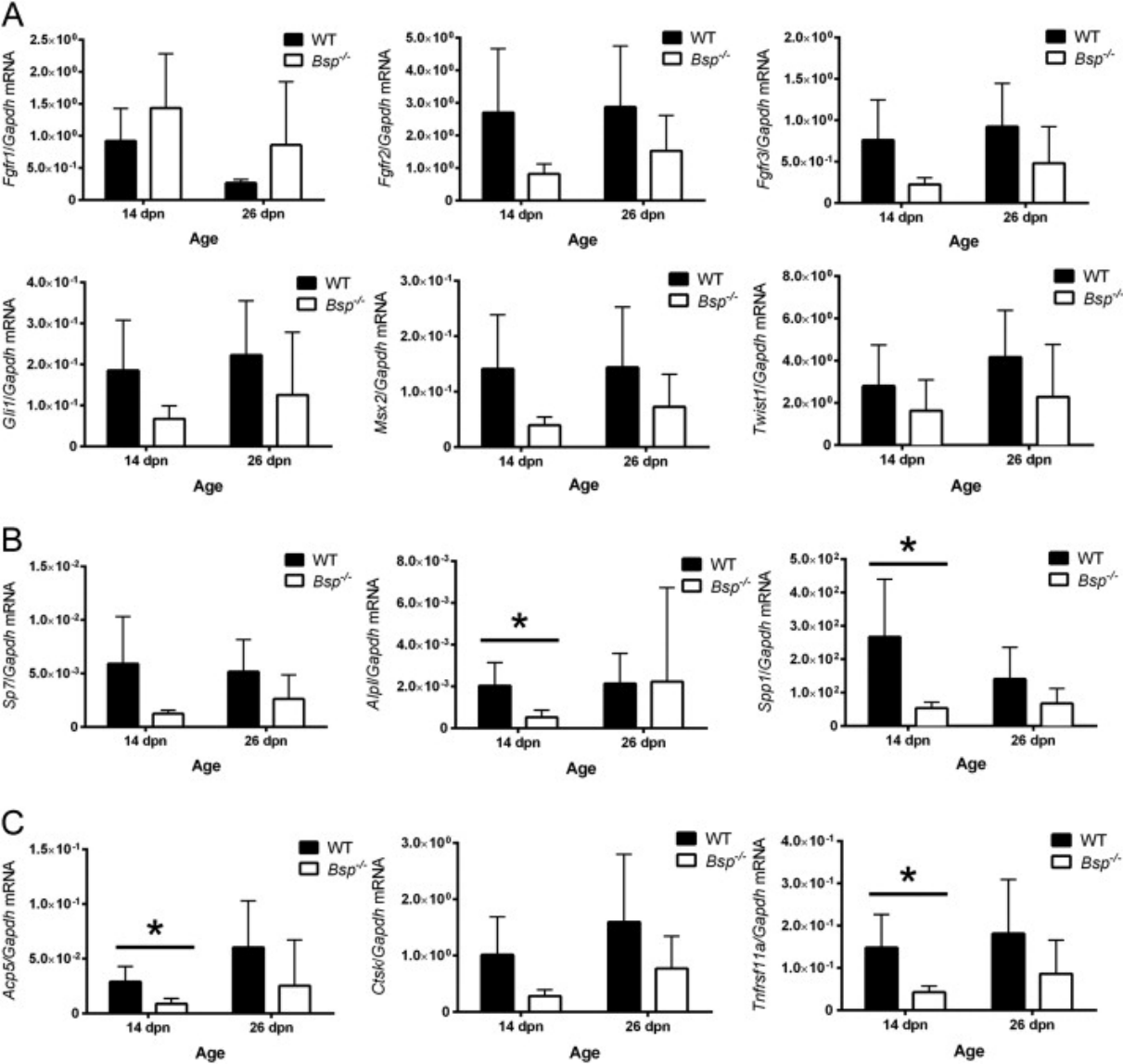
* p < 0.05 by independent samples t-test

** p < 0.01 by independent samples t-test

Supplementary Table 2. Craniofacial parameters of *Bsp*^{-/-} versus WT mice. Craniofacial measurements were made on 3D microCT reconstructions of WT and *Bsp*^{-/-} mice at 5, 14, and 26 dpn (n=4-5 for each genotype and age). Values are reported as mean ± SD.

	5 dpn		14 dpn		26 dpn	
	WT	<i>Bsp</i> ^{-/-}	WT	<i>Bsp</i> ^{-/-}	WT	<i>Bsp</i> ^{-/-}
Skull length (mm)	13.12 ± 0.50	12.74 ± 1.16	17.33 ± 0.37	17.14 ± 0.39	18.62 ± 0.59	19.24 ± 0.54
Nose length (mm)	7.79 ± 0.45	7.46 ± 1.02	10.30 ± 0.32	10.25 ± 0.37	11.72 ± 0.44	12.27 ± 0.35
Nasal bone length (mm)	3.17 ± 0.21	2.89 ± 0.44	5.03 ± 0.31	4.84 ± 0.27	5.79 ± 0.35	6.27 ± 0.27
Frontal bone length (mm)	4.60 ± 0.28	4.38 ± 0.54	5.25 ± 0.26	5.41 ± 0.19	5.94 ± 0.20	6.00 ± 0.11
Parietal bone length (mm)	2.43 ± 0.25	2.26 ± 0.26	3.76 ± 0.10	3.68 ± 0.05	4.14 ± 0.26	4.23 ± 0.13
Upper jaw length (mm)	6.85 ± 0.23	6.66 ± 0.41	9.55 ± 0.25	9.90 ± 0.19	10.91 ± 0.23	11.31 ± 0.24
Premaxilla width (mm)	3.68 ± 0.13	3.89 ± 0.53	3.73 ± 0.04	3.66 ± 0.10	3.75 ± 0.08	3.84 ± 0.08
Lacrymal width (mm)	3.38 ± 0.06	3.43 ± 0.12	3.38 ± 0.03	3.35 ± 0.03	3.29 ± 0.04	3.32 ± 0.04
Squamosal width (mm)	8.21 ± 0.27	7.77 ± 0.25	10.11 ± 0.33	9.85 ± 0.25	10.45 ± 0.37	10.58 ± 0.27
Skull width (mm)	8.02 ± 0.37	7.73 ± 0.51	9.95 ± 0.19	10.15 ± 0.05*	10.01 ± 0.13	10.15 ± 0.04
Skull height (mm)	5.10 ± 0.15	5.13 ± 0.61	6.06 ± 0.06	6.09 ± 0.03	6.14 ± 0.18	6.24 ± 0.11

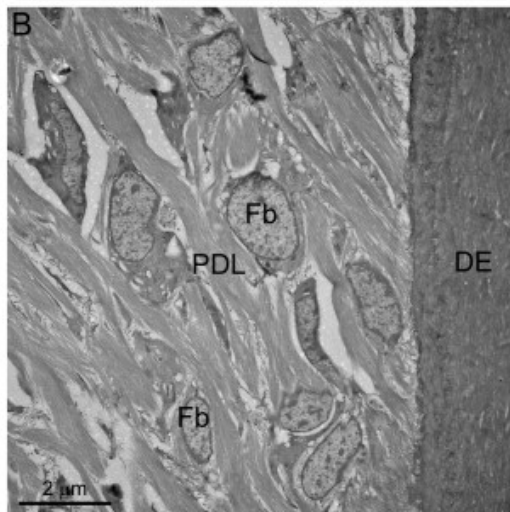
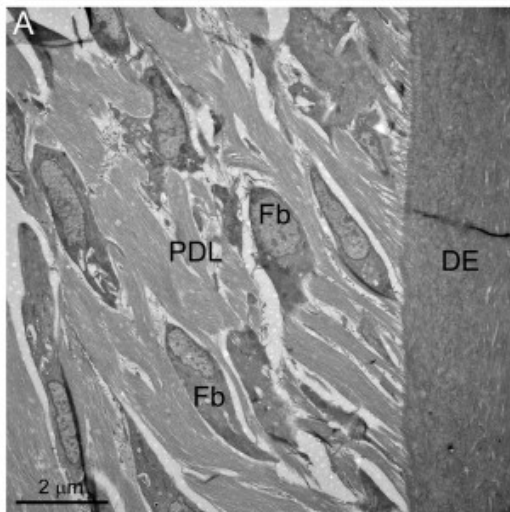
* p < 0.05 by independent samples t-test



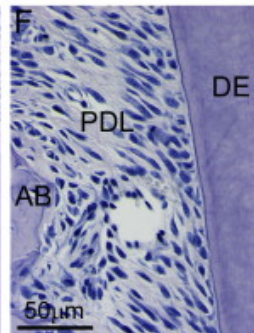
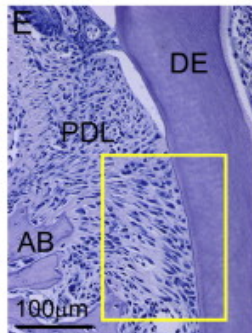
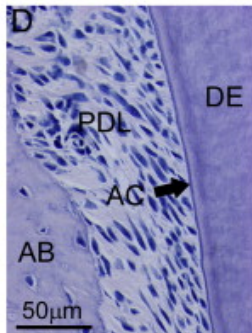
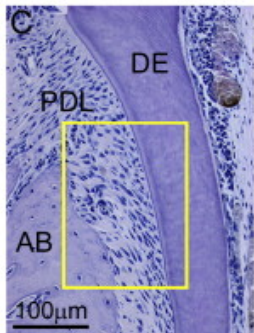
Control

Bsp^{-/-} mouse

TEM



H&E



Control

Bsp^{-/-} mouse